The Meteoritical Society

Meteoritics & Planetary Science 47, Nr 11, 1809–1829 (2012)
doi: 10.1111/maps.12021

Large silica-rich igneous-textured inclusions in the Buzzard Coulee chondrite: Condensates, differentiates, or impact melts?

Alex RUZICKA[1*], Melinda HUTSON[1], Christine FLOSS[2], and Alan HILDEBRAND[3]

[1]Cascadia Meteorite Laboratory and Department of Geology, Portland State University, 17 Cramer Hall, 1721 SW Broadway, Portland, Oregon 97207–0751, USA
[2]Laboratory for Space Sciences and Physics Department, Washington University, Campus Box 1105, St. Louis, Missouri 63130, USA
[3]Department of Geosciences, University of Calgary, 2500 University Drive NW, Calgary, Alberta T2N1N4, Canada
[*]Corresponding author. E-mail: ruzickaa@pdx.edu

(Received 17 January 2012; revision accepted 05 October 2012)

Abstract–We studied three large (2–4 mm diameter) igneous-textured inclusions in the Buzzard Coulee (H4) chondrite using microanalytical techniques (OLM, SEM, EMPA, SIMS) to better elucidate the origins of igneous inclusions in ordinary chondrites. The inclusions are clasts that come in two varieties (1) white inclusions Bz-1 and Bz-2 represent a nearly holocrystalline assemblage of low-Ca and high-Ca pyroxene (63–66 area%) and cristobalite (33–36%) and (2) tan inclusion Bz-3 is glass-rich (approximately 60%) with low-Ca and high-Ca pyroxene phenocrysts. The bulk compositions of the inclusions determined by modal reconstruction are all SiO_2-rich (approximately 67 wt% for Bz-1 and Bz-2, approximately 62% for Bz-3), but Bz-3 is enriched in incompatible elements (e.g., REE approximately 4–5 × CI abundances), whereas Bz-2 and Bz-1 are depleted in those elements that are most incompatible in pyroxene (e.g., La-Ho approximately 0.15–0.4 × CI abundances). These bulk compositions do not resemble what one would expect for partial or complete shock melting of a chondritic precursor, and show no evidence for overall volatility control. We infer that the inclusions originated through igneous differentiation and FeO reduction, with Bz-3 forming as an "andesitic" partial melt (approximately 30–40% partial melting of an H chondrite precursor), and Bz-1 and Bz-2 forming as pyroxene-cristobalite cumulates from an Si-rich melt. We suggest that both types of melts experienced a period of transit through a cold, low-pressure space environment in which cooling, FeO reduction, and interaction with a vapor occurred. Melts may have been lofted into space by excavation or splashing during collisions, or by pyroclastic volcanism. Our results indicate intriguing similarities between the inclusions in Buzzard Coulee and the silicates in some iron (IIE-type) and stony iron (IVA-type) meteorites, suggesting a genetic relationship.

INTRODUCTION

Approximately 4% of ordinary chondrites contain large igneous-textured inclusions ≥5 mm and up to 4 cm across (Bridges and Hutchison 1997), and approximately 29% contain at least one inclusion ≥2–3 mm across, which solidified from melt volumes one to six orders of magnitude larger than typical chondrules in the meteorites. The inclusions have a variety of shapes, textures, and compositions, but are almost always metal- and sulfide-poor (Bridges and Hutchison 1997; Ruzicka et al. 1998, 2000). Some objects are clasts derived from larger rocks, whereas others crystallized as large melt droplets ("macrochondrules"—Bridges and Hutchison 1997; or "megachondrules"—Ruzicka et al. 1998, 2000). Still others are neither obvious clasts nor megachondrules and have been termed "large igneous-textured enclaves" or LITEs (Jamsja and Ruzicka 2010). Some inclusions are silica-rich and these tend to be enriched in ^{18}O and often ^{17}O compared with other ordinary chondrite material (Bridges et al. 1995, 1998; Ruzicka et al. 1995, 2000).

Various origins have been proposed for large inclusions. The inclusions may have formed as (1) shock melts (Dodd and Jarosewich 1976; Fodor and Keil 1976; Keil et al. 1980; Rubin et al. 1981; Boctor et al. 1982; Ruzicka et al. 1998, 2000; Jamsja and Ruzicka 2010); (2) melts of vapor-fractionated condensate mixtures (Ruzicka et al. 1998, 2000); or as (3) differentiates derived from once-molten planetesimals (Hutchison et al. 1988; Kennedy et al. 1992; Bridges et al. 1995; Ruzicka et al. 1995). The megachondrules probably formed by processes analogous to those which formed chondrules although involving much larger melt production (Binns 1967; Bridges and Hutchison 1997; Ruzicka et al. 1998), but the situation is less clear for other objects. Regardless of how the inclusions formed, it appears that relatively large-scale melting processes are recorded in meteorites that are themselves undifferentiated.

The Buzzard Coulee chondrite (H4 S2 W0, glass-bearing and therefore borderline petrographic type 3), which fell in November 2008 (Hutson et al. 2009; Weisberg et al. 2009) contains at least two types of inclusions visible in hand specimens. This provides an opportunity for further studies of inclusions in a weakly metamorphosed, lightly shocked, and minimally weathered chondrite. Both types of inclusions are typically subangular to subrounded and vary in diameter from approximately 1 cm down to much smaller sizes. The most common type has a vitreous to chalky white appearance (Munsell system N8 to N9) and is hereafter referred to as a "white" inclusion; the other is light brownish to yellowish grey (5YR 6/1 to 5Y 7/2) and is hereafter referred to as a "tan" inclusion. In a total area surveyed of approximately 79 cm^2, 16 white and tan inclusions >0.25 mm in diameter were found. Some Buzzard Coulee specimens show a faint breccia texture (Hildebrand et al. 2009; Hutson et al. 2009; Higgins et al. 2011), and in such cases, the inclusions occur in the finer grained, interclast portions.

In this study, we used microanalytical techniques to study three examples of the two inclusion types in Buzzard Coulee to place constraints on their origin.

METHODS AND SAMPLES

Polished thin sections were prepared of three inclusions (Bz-1, Bz-2, and Bz-3, respectively) identified in two different specimens of Buzzard Coulee (Table 1). The inclusions were examined using optical light microscopy (OLM) and scanning electron microscopy (SEM) techniques at Portland State University using a Leica DM 2500 petrographic microscope, a JEOL 35C SEM, and a Zeiss Sigma FE-VP SEM. Phases were analyzed for major elements by electron microprobe analysis (EMPA) using a Cameca SX-100 electron microprobe housed at Oregon State University and accessed remotely from Portland State University, and for trace elements by secondary ion mass spectrometry (SIMS) using the modified Cameca ims-3f ion probe at Washington University. Bulk compositions were calculated by modal reconstruction, combining SEM data for phase proportions with EMPA and SIMS phase analyses. Further details on experimental procedures and methods are given in the Appendix.

Table 1. Modal compositions (area %) of inclusions in Buzzard Coulee.

	Bz-1[a]	Bz-2[b]	Bz-3[c]
Low-Ca pyroxene	53.6	47.8	9.4
High-Ca pyroxene	12.8	15.4	27.4
Cristobalite	33.3	35.5	–
Feldspar	0.2[d]	1.3[e]	2.5[f]
Na-rich glass	–	–	57.1[g]
K-rich glass	–	–	2.9[h]
Olivine	0.1	<0.1	0.6

[a]White inclusion 1 in section BC2, Rock 1. Based on 158,293 classified pixels; omits 130,177 unclassified pixels.
[b]White inclusion 2 in section CML0481A, Rock 2. Based on 672,268 classified pixels; omits 211,115 unclassified pixels.
[c]Tan inclusion 3 in section CML0481B, Rock 2. Based on 231,852 classified pixels; omits 135,805 unclassified pixels.
[d]Feldspathic phase with average composition approximately $Ab_{65}Or_4An_{31}$.
[e]Feldspathic phase with average composition approximately $Ab_{64}Or_3An_{33}$.
[f]Feldspar with average composition approximately $Ab_{76}Or_2An_{22}$.
[g]Feldspathic glass with average composition approximately $Ab_{72}Or_{12}An_{16}$.
[h]Feldspathic glass with average composition approximately $Ab_{47}Or_{44}An_9$.

RESULTS

Petrography

Images of the three inclusions we studied are shown in Fig. 1, and modal data are presented in Table 1. Bz-1 and Bz-2 are white inclusions, and Bz-3 is a tan inclusion (Fig. 1a). Despite being found in different hand specimens, Bz-1 and Bz-2 have very similar modes and textures and appear to be fragments of the same, nearly holocrystalline, lithology, composed of pyroxene (approximately 63–66%) + silica polymorph (approximately 33–36%) (Table 1). The latter polymorph was confirmed by EBSD techniques to be cristobalite. Bz-3 is clearly different as it contains abundant glass (approximately 60%) (Table 1).

White Inclusion Bz-2

Bz-2 (diameter in thin section approximately 2.2×3.6 mm) is primarily composed of elongate low-Ca pyroxene grains typically approximately 100×190 μm across, and small (<20–30 μm across) cristobalite grains that form compact aggregates typically approximately 120–340 μm in diameter (Figs. 1b and 1e). In one portion of Bz-2, these aggregates form bars between adjacent

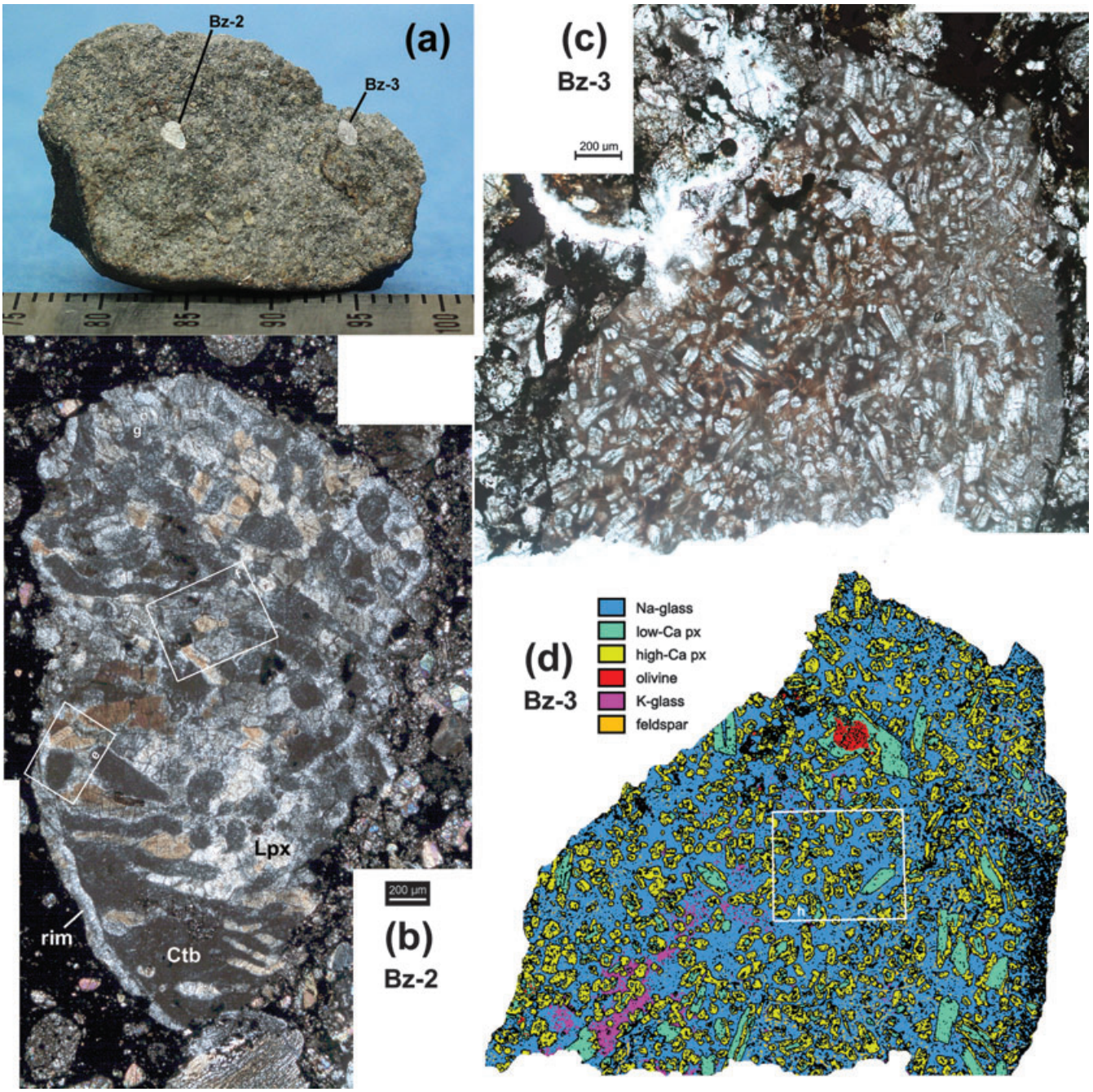

Fig. 1. Images of inclusions in Buzzard Coulee. a) Hand specimen image of Buzzard Coulee (Rock 2) showing Bz-2 and Bz-3. The ruler at bottom has small divisions equal to 1 mm. b) Cross-polarized transmitted light micrograph centered on Bz-2 showing a partial rim of pyroxene (lower left) and a broken margin elsewhere. Cristobalite (Ctb) aggregates appear dark grey; low-Ca pyroxene (Lpx) appears brown (orthobronzite) or white to grey (orthobronzite and clinobronzite). Boxes show the locations of e (left), f (center), and g (barely visible as a small area near the top). c) Plane-polarized transmitted light micrograph centered on Bz-3 showing crystals of pyroxene embedded in a red-brown feldspathic glass. White areas at the bottom and upper left are epoxy. d) Colorized phase map of Bz-3 derived from SEM data. One grain of olivine (red) occurs at top center encased in pyroxene; most glass is Na-rich, but one area is K-rich (lower left). The box shows the region in h.

aligned low-Ca pyroxene grains before merging into an approximately 0.6 × 1 mm cristobalite-rich area adjacent to an inclusion rim (Fig. 1b). Low-Ca pyroxene grains are mainly orthobronzite, but twinned clinobronzite is also present (Fig. 1f). In some areas, clinobronzite partly surrounds orthobronzite, whereas the reverse is true

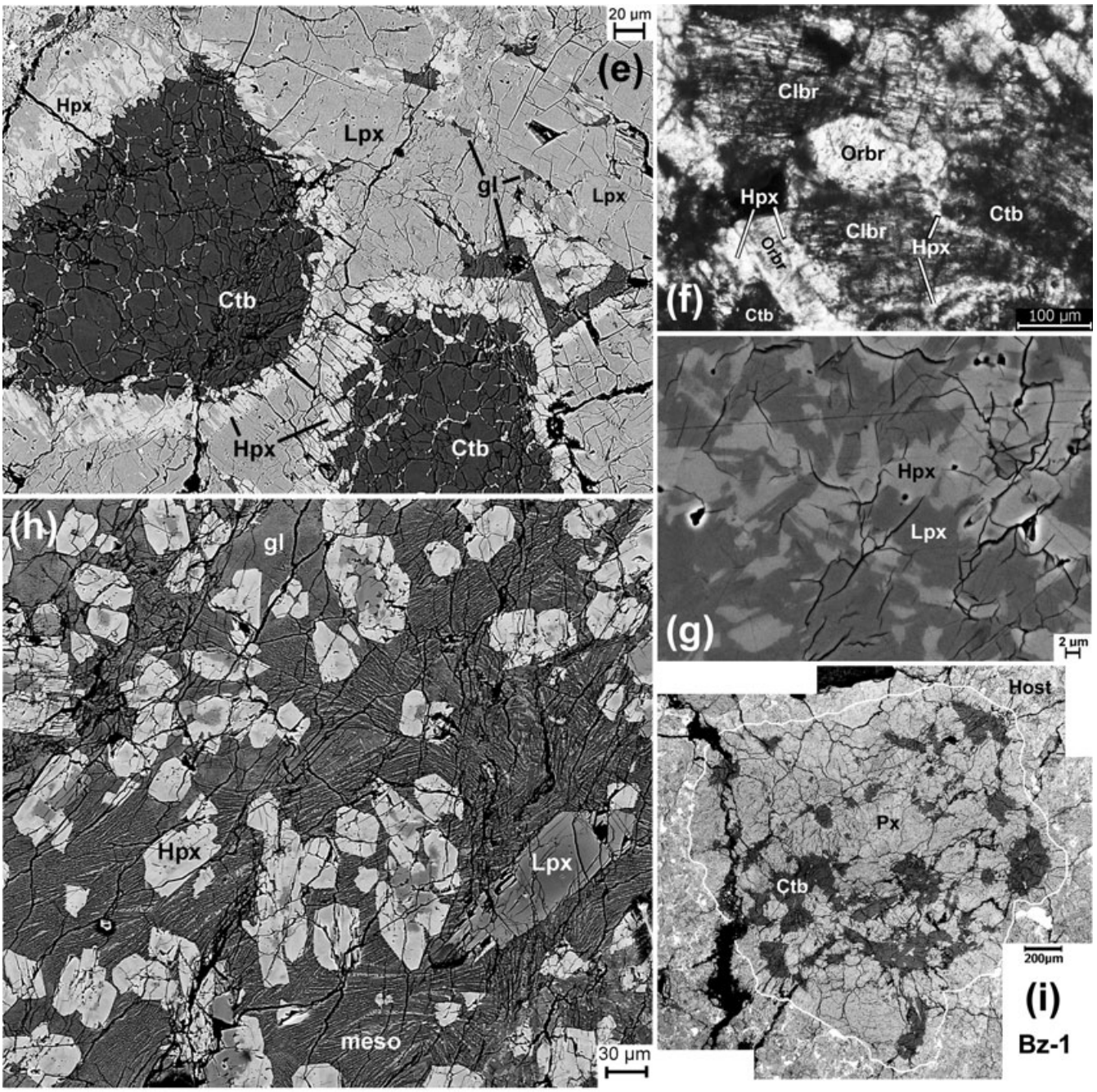

Fig. 1. *Continued.* e) Backscattered electron (BSE) image of Bz-2 showing Lpx, aggregates of Ctb, minor glass (gl), and high-Ca pyroxene (Hpx). Light vein-like areas within Ctb are Hpx. The inclusion edge is at extreme upper left and is marked by an irregular fracture (black). Lpx + Hpx intergrowths form rims on Ctb aggregates. f) Cross-polarized transmitted light micrograph of Bz-2 showing orthobronzite (Orbr), twinned clinobronzite (Clbr), Ctb aggregates, and Hpx rims on Orbr, Clbr and Ctb. g) High-magnification BSE image of low-Ca pyroxene grain core in Bz-2 showing a fine intergrowth of Lpx and Hpx. h) BSE image of Bz-3 showing pyroxene phenocrysts set in glass and a mesostasis (meso) of plagioclase + pyroxene. Hpx often forms overgrowths on Lpx. i) BSE image mosaic of Bz-1 (outlined) showing the presence of pyroxene (Px) and Ctb, and an almost complete absence of metal or sulfide (bright spots in host). Black areas are cracks and holes in the section.

elsewhere. High-Ca pyroxene is present as thin selvages between individual silica grains in the cristobalite aggregates (Fig. 1e), and is intergrown with low-Ca pyroxene in a variety of textural settings. These intergrowths form Ca-rich rims on cristobalite aggregates (Fig. 1e) and on low-Ca pyroxene grains (Figs. 1e and 1f).

In some pyroxene grains, high- and low-Ca pyroxene form fine (< 10 μm) scale intergrowths far from grain margins (Fig. 1g). In all these intergrowths, high-Ca pyroxene is enclosed within optically continuous low-Ca pyroxene. Feldspathic areas consisting of glass and feldspar are minor in Bz-2 (1.3 area % overall), and are located interstitial to other grains, commonly pyroxene (Fig. 1e).

The inclusion has what appears to be a partial rim of low-Ca pyroxene + high-Ca pyroxene (approximately 80–120 μm wide), which separates cristobalite from the host chondrite (Fig. 1b). In detail, however, this rim has an identical texture to rims around cristobalite aggregates (Fig. 1e), suggesting that it does not represent a special boundary. Rather, this edge of the inclusion appears to represent the merged rims of cristobalite aggregates. Elsewhere the inclusion has a clearly brecciated margin (grains of pyroxene and cristobalite are truncated), indicating that Bz-2 is a clast.

White Inclusion Bz-1

Bz-1 (diameter in thin section approximately 2.0 × 2.1 mm) is petrographically similar to Bz-2. It consists primarily of cristobalite aggregates (approximately 70–380 μm across) and pyroxene (Fig. 1i). High-Ca pyroxene is present in rims on low-Ca pyroxene and on cristobalite aggregates; glass or feldspar is rare (approximately 0.2 area%). Silica aggregates are equant to elongate, with barred textures less developed than in Bz-2 (Fig. 1i). As with Bz-2, the inclusion has an irregular, apparently brecciated outline and is therefore a clast (Fig. 1i).

Tan Inclusion Bz-3

Bz-3 (diameter approximately 2.1 × 3.2 mm, estimated from thin section and hand specimen) has a microporphyritic texture composed of pyroxene set in a groundmass of red-brown glass with pyroxene and plagioclase crystallites (Figs. 1c and 1h). Low-Ca pyroxene phenocrysts are primarily orthoenstatite (but at least one clinoenstatite grain is present) and form elongate grains (approximately 20–70 μm wide × approximately 40–190 μm long). These grains often have partial or complete overgrowths (approximately 7–50 μm wide) of high-Ca pyroxene, although some low-Ca pyroxene grains lack overgrowths (Figs. 1d and 1h). High-Ca pyroxene also forms isolated or grouped phenocrysts (approximately 70–120 μm across). A single grain of olivine (approximately 140 μm across) is present, which itself is completely overgrown by low-Ca pyroxene (Fig. 1d). Most of the glass is Na-rich, although a portion is K-rich (Fig. 1d). This division into Na- and K-rich glass resembles what has been found in silicate inclusions from the Sombrerete ungrouped iron (Ruzicka et al. 2006). In some areas, pyroxene phenocrysts are broken at the inclusion edge, indicating that Bz-3 is a clast.

Mineral Chemistry

Tables 2 and 3 present EMPA and SIMS mineral–chemical data. Major-element compositions for pyroxene and olivine are shown in Fig. 2, and trace-element abundances for various phases are plotted in Figs. 3 and 4 (for Bz-2 and Bz-3 only, as Bz-1 was not analyzed with SIMS).

EMPA Results

Pyroxene compositions in Bz-1 and Bz-2 are similar to one another and to chondrules in Buzzard Coulee, with analyses forming an apparent mixing array between low-Ca pyroxene (approximately $Wo_{0.5–4}$ $En_{81–85}$ $Fs_{15–18}$) and diopside (approximately $Wo_{44–47}$ $En_{48–51}$ $Fs_{4–6}$) (Fig. 2). Within this range, pyroxene grains in Bz-1 are slightly more ferrous than in Bz-2 (Fig. 2b; Table 2). Cristobalite in both inclusions is nearly pure SiO_2, with the major impurity being FeO (approximately 0.1–0.5 wt%).

Bz-3 has distinctly magnesian pyroxene and olivine compared with grains elsewhere in the meteorite. In this inclusion, olivine is $Fa_{9.8 \pm 0.1}$ compared with $Fa_{17.8 \pm 0.3}$ elsewhere, and low-Ca pyroxene ($Wo_{1.2 \pm 0.5}$ $En_{90.4 \pm 2.4}$ $Fs_{8.4 \pm 2.1}$) is less ferrous than elsewhere (Fig. 2). This indicates that Bz-3 is in disequilibrium with the rest of the meteorite and that Buzzard Coulee must be a breccia that was not significantly metamorphosed following final agglomeration. Most high-Ca pyroxene in Bz-3 is augite ($Wo_{20–40}$), although some is pigeonite ($Wo_{5–14}$) (Fig. 2b).

SIMS Results for Bz-2

Trace element abundances for Bz-2 are shown in Fig. 3. Diopside and orthobronzite show fractionated patterns, with negative Eu anomalies and enrichments in HREE (Fig. 3a). In contrast, two analyses of clinobronzite in Bz-2 show an overall flat REE pattern with irregularities and no negative Eu anomaly (Fig. 3b). Measured concentrations of most elements in clinobronzite are intermediate to diopside and orthobronzite, except for enrichments in elements that should concentrate in a feldspathic fraction (Na, Al, K, Rb, Sr, Ba) or in chromite (V, Cr). It is possible therefore that these analyses reflect the presence of glass and chromite inclusions, but it seems unlikely that the relatively unfractionated pattern can be fully explained this way. Two analyses centered on glassy feldspathic patches (which slightly overlap surrounding pyroxene) indicate that the glass has a positive Eu anomaly and is enriched compared with orthobronzite and diopside in incompatible elements such as Na, Al, K, Ti, Rb, Sr, and Ba (Fig. 3c). Abundances in cristobalite are low (0.01–0.1 × CI) for virtually all measured elements, except for Ca (approximately 0.25 × CI) and Si (Fig. 3c). Except for Si

Table 2. EMPA results for inclusion phase compositions.[a]

	Bz-1 Low-Ca pyroxene	Bz-1 High-Ca pyroxene	Bz-1 cristobalite	Bz-2 Low-Ca pyroxene[b]	Bz-2 High-Ca pyroxene[c]	Bz-2 cristobalite	Bz-3 Low-Ca pyroxene	Bz-3 High-Ca pyroxene	Bz-3 K-rich glass	Bz-3 olivine
Mol%										
Fa										9.8 (0.1)
Wo	1.7 (0.4)	27.0 (14.7)		0.9 (0.1)	45.6 (0.7)		1.2 (0.5)	26.2 (10.3)		
En	81.2 (0.8)	62.3 (11.1)		83.2 (0.6)	49.2 (0.7)		90.4 (2.4)	69.6 (9.2)		
Fs	17.1 (0.5)	10.7 (3.7)		15.9 (0.5)	5.2 (0.1)		8.4 (2.1)	4.2 (2.4)		
wt%										
SiO_2	55.6 (0.6)	54.4 (0.5)	99.3 (0.5)	55.1 (0.70)	53.1 (0.6)	98.2 (1.0)	56.3 (0.4)	54.6 (1.0)	69.1 (0.9)	40.2 (0.4)
TiO_2	*0.04* (*0.01*)	0.09 (0.04)	*0.01* (*0.02*)	0.07 (0.04)	0.09 (0.02)	*0.01*	0.13 (0.04)	0.18 (0.07)	0.49 (0.22)	*0.01* (*0.01*)
Al_2O_3	0.21 (0.10)	0.26 (0.07)	0.07 (0.03)	0.10 (0.18)	0.18 (0.05)	0.04 (0.03)	0.23 (0.23)	1.05 (0.83)	17.9 (0.6)	0.05 (0.08)
Cr_2O_3	0.20 (0.11)	0.51 (0.29)	*0.01* (*0.01*)	0.28 (0.51)	0.65 (0.07)	*0.01* (*0.01*)	*0.08* (*0.04*)	0.24 (0.08)	*0.01* (*0.01*)	*0.02* (*0.02*)
FeO	11.1 (0.3)	6.79 (2.43)	0.38 (0.11)	10.7 (0.3)	3.28 (0.11)	0.14 (0.05)	5.75 (1.37)	2.73 (1.60)	0.44 (0.22)	9.48 (0.24)
MnO	0.51 (0.03)	0.34 (0.09)	*0.01* (*0.02*)	0.49 (0.02)	0.21 (0.02)	*0.02* (*0.01*)	0.49 (0.02)	0.41 (0.07)	*0.03* (*0.01*)	0.43 (0.02)
MgO	29.5 (0.6)	22.1 (4.3)	0.10 (0.03)	31.4 (0.5)	17.5 (0.4)	0.06 (0.10)	34.7 (1.2)	25.4 (4.0)	2.81 (1.24)	48.7 (0.7)
NiO	*0.01* (*0.03*)	*0.03* (*0.02*)	*0.01* (*0.02*)	*0.03* (*0.02*)	*0.01* (*0.04*)	*0.04* (*0.02*)	*0.02* (*0.02*)	0.02 (0.02)	*0.02*	*0.04* (*0.03*)
CaO	0.84 (0.21)	13.2 (7.0)	0.13 (0.03)	0.48 (0.04)	22.5 (0.2)	0.07 (0.11)	0.65 (0.26)	13.2 (5.2)	0.59 (0.05)	0.04 (0.04)
Na_2O	*0.04* (*0.01*)	0.28 (0.14)	*0.02* (*0.01*)	*0.02* (*0.02*)	0.40 (0.06)	0.01 (0.01)	0.04 (0.10)	0.34 (0.30)	1.58 (0.07)	*0.02* (*0.03*)
K_2O	< 0.01	< 0.01	*0.01* (*0.00*)	n.a.	n.a.	n.a.	n.a.	n.a.	5.61 (0.59)	n.a.
Total	98.0	97.9	100.02	98.6	97.9	98.6	98.4	98.2	98.6	98.9
N	9	7	5	80	8	21	13	18	2	6
T_{app} (°C)	851 ± 63	≥ 763		752 ± 15	747 ± 47		831 ± 61	> 1100		

[a]Mean values; standard deviation of the mean shown in parentheses.

[b]Low Wo (< 1.1) population only.

[c]High Wo (> 44.1) population only.

N = number of analyses; n.a. = not analyzed; T_{app} = apparent 2-pyroxene geothermometer temperature. Values in italics are below 3σ calculated background.

Table 3. SIMS results for phase compositions in inclusions Bz-2 and Bz-3.[a]

	(1) Bz-2 avg. low-Ca px ORBR	(2) Bz-2 low-Ca px CLBR A7-3	(3) Bz-2 avg. high-Ca px	(4) Bz-2 avg. cristobalite	(5) Bz-3 avg. low-Ca px[b]	(6) Bz-3 avg. high-Ca px[c]	(7) Bz-3 fractionated low-Ca px B11-6	(8) Bz-3 Na-rich glass B11-3	(9) Bz-3 K-rich glass B12-1
N	3		3	3	3	3			
Na μg g^{-1}	308 (309)	1876 (2)	1460 (360)	70.5 (7.8)	3500 (2990)	13400 (3690)	1503 (2)	57350 (30)	30660 (15)
Mg wt%	16.0 (0.2)	14.73 (0.01)	11.1 (1.5)	0.262 (0.059)	15.4 (1.0)	9.57 (1.66)	16.19 (0.01)	14.46 (0.01)	2.898 (0.002)
Al wt%	0.0751 (0.0578)	0.3327 (0.0002)	0.0554 (0.0139)	0.0146 (0.0129)	0.569 (0.460)	1.74 (0.47)	0.3686 (0.0003)	n.a.	n.a.
Si wt%	25.7 (0.1)	24.45 (0.01)	25.0 (0.5)	45.9 (0.5)	26.21 (0.09)	25.2 (0.3)	26.43 (0.01)	29.17 (0.01)	29.05 (0.01)
P μg g^{-1}	42.5 (38.8)	15.6 (0.4)	17.8 (6.3)	21.8 (18.8)	14.0 (7.5)	27.1 (20.6)	13.4 (0.5)	31.7 (0.8)	32.2 (0.7)
K μg g^{-1}	35.7 (55.2)	261 (1)	19.6 (5.2)	9.67 (3.48)	916 (821)	5090 (1840)	592 (1)	34780 (20)	94280 (40)
Ca wt%	0.306 (0.036)	0.782 (0.011)	6.97 (1.73)	0.239 (0.052)	0.433 (0.235)	6.13 (0.91)	1.03 (0.02)	11.81 (0.01)	3.09 (0.01)
Sc μg g^{-1}	0.866 (0.192)	1.00 (0.14)	20.6 (8.5)	0.259 (0.170)	10.4 (1.0)	40.2 (4.9)	17.5 (0.3)	12.0 (0.2)	20.1 (0.2)
Ti μg g^{-1}	312 (143)	577 (1)	388 (150)	33.4 (1.2)	593 (99)	1300 (250)	581 (2)	2819 (3)	3346 (3)
V μg g^{-1}	47.8 (6.7)	83.7 (0.3)	58.2 (27.1)	1.61 (0.51)	6.64 (1.71)	7.03 (0.70)	8.19 (0.14)	4.38 (0.10)	4.13 (0.09)
Cr μg g^{-1}	3210 (220)	4320 (3)	2550 (490)	95.7 (19.4)	484 (43)	1190 (220)	799 (2)	40.1 (0.4)	277 (1)
Mn μg g^{-1}	3680 (350)	3431 (3)	2190 (330)	42.5 (10.9)	2860 (220)	2110 (330)	3236 (4)	236 (1)	533 (1)
Fe wt%	5.67 (0.69)	5.16 (0.01)	3.56 (0.61)	0.273 (0.033)	2.43 (0.18)	1.82 (1.19)	2.14 (0.01)	0.369 (0.003)	0.694 (0.004)
Co μg g^{-1}	6.13 (0.77)	4.61 (0.15)	6.95 (0.98)	3.48 (0.45)	4.79 (0.42)	6.26 (0.16)	5.09 (0.24)	2.54 (0.12)	3.33 (0.13)
Ni μg g^{-1}	12.3 (1.4)	14.9 (1.4)	53.0 (23.5)	8.75 (4.12)	76.7 (13.0)	152 (34)	67.9 (3.9)	60.1 (3.7)	134 (6)
Rb μg g^{-1}	0.0938 (0.0135)	1.06 (0.18)	0.682 (0.472)	0.118 (0.015)	3.48 (2.29)	19.8 (6.3)	2.45 (0.21)	112 (1)	353 (2)
Sr μg g^{-1}	0.342	2.13 (0.27)	1.84 (0.22)	0.196 (0.118)	3.11 (2.48)	10.8 (4.2)	1.40 (0.62)	16.1 (7.2)	30.7 (8.0)
Y μg g^{-1}	0.128 (0.052)	0.229 (0.024)	2.05 (0.57)	0.0263 (0.0083)	1.69 (0.36)	6.58 (1.10)	1.67 (0.09)	7.13 (0.43)	9.85 (0.47)
Zr μg g^{-1}	0.754 (0.459)	0.686 (0.042)	14.8 (4.7)	0.219 (0.201)	3.30 (1.29)	8.86 (2.54)	2.14 (0.13)	32.8 (1.2)	40.1 (1.3)
Ba μg g^{-1}	0.119 (0.112)	0.439 (0.029)	0.166 (0.076)	0.168 (0.115)	1.41 (0.91)	3.95 (0.65)	0.513 (0.036)	19.8 (0.4)	24.3 (0.4)
La μg g^{-1}	0.0191 (0.0006)	0.028 (0.003)	0.106 (0.042)	0.00717 (0.00360)	0.216 (0.062)	0.491 (0.105)	0.277 (0.013)	1.28 (0.07)	1.45 (0.05)
Ce μg g^{-1}	0.0601 (0.0282)	0.0826 (0.0073)	0.346 (0.099)	0.0240 (0.0049)	0.683 (0.226)	1.51 (0.33)	0.941 (0.051)	3.22 (0.14)	3.83 (0.11)
Pr μg g^{-1}	0.0069 (0.0027)	0.0148 (0.0013)	0.0636 (0.0130)	0.0028	0.0898 (0.0410)	0.275 (0.061)	0.160 (0.012)	0.393 (0.025)	0.520 (0.025)
Nd μg g^{-1}	0.0241 (0.0042)	0.0566 (0.0035)	0.289 (0.075)	0.0109	0.402 (0.151)	1.47 (0.36)	0.741 (0.029)	1.96 (0.07)	2.74 (0.07)
Sm μg g^{-1}	0.00815 (0.00375)	0.0185 (0.0030)	0.159 (0.056)	b.d.	0.143 (0.069)	0.658 (0.139)	0.314 (0.023)	0.264 (0.029)	0.591 (0.032)
Eu μg g^{-1}	0.001 (0.0006)	0.0101 (0.0011)	0.0216 (0.0039)	b.d.	0.0174 (0.0120)	0.0822 (0.0260)	0.0281 (0.0034)	0.182 (0.021)	0.248 (0.016)
Gd μg g^{-1}	0.0172 (0.0095)	0.0169 (0.0038)	0.168 (0.039)	b.d.	0.188 (0.086)	0.926 (0.228)	0.211 (0.026)	0.806 (0.071)	1.31 (0.07)
Tb μg g^{-1}	0.0026 (0.0015)	0.0059 (0.001)	0.0400 (0.0151)	b.d.	0.0365 (0.0222)	0.165 (0.031)	0.0326 (0.0053)	0.144 (0.015)	0.224 (0.013)
Dy μg g^{-1}	0.0208 (0.0068)	0.0349 (0.0029)	0.347 (0.112)	0.0025	0.285 (0.111)	1.20 (0.13)	0.300 (0.016)	1.24 (0.05)	1.77 (0.05)
Ho μg g^{-1}	0.00507 (0.00040)	0.0074 (0.001)	0.0830 (0.0217)	0.0007	0.0593 (0.0249)	0.254 (0.037)	0.065 (0.006)	0.285 (0.022)	0.385 (0.014)
Er μg g^{-1}	0.0218 (0.0092)	0.0331 (0.0025)	0.285 (0.079)	0.0034	0.234 (0.069)	0.840 (0.101)	0.198 (0.013)	0.883 (0.040)	1.28 (0.037)
Tm μg g^{-1}	0.00357 (0.00172)	0.0068 (0.001)	0.0500 (0.0118)	0.0007	0.0356 (0.0061)	0.115 (0.027)	0.0415 (0.0048)	0.126 (0.010)	0.176 (0.011)
Yb μg g^{-1}	0.0384 (0.0148)	0.0597 (0.0055)	0.421 (0.107)	0.0081	0.326 (0.035)	1.11 (0.24)	0.700 (0.033)	0.163 (0.021)	0.715 (0.034)
Lu μg g^{-1}	0.0056 (0.0024)	0.0079 (0.0013)	0.0633 (0.0149)	0.0006	0.0515 (0.0101)	0.141 (0.012)	0.0364 (0.0057)	0.127 (0.016)	0.235 (0.015)

[a]Includes average (mean) values in columns (1), (3), (4), (5), (6), and individual analyses in columns (2), (7), (8), (9); values in parentheses are standard deviations for means, or 1σ counting statistic error for individual analyses; b.d. = below detection (apparent concentration ≤ 1σ counting statistic error); px = pyroxene; ORBR = orthobronzite; CLBR = clinobronzite; other symbols same as in Table 1.

[b]Excludes analysis B11-6.

[c]Excludes analysis B11-7.

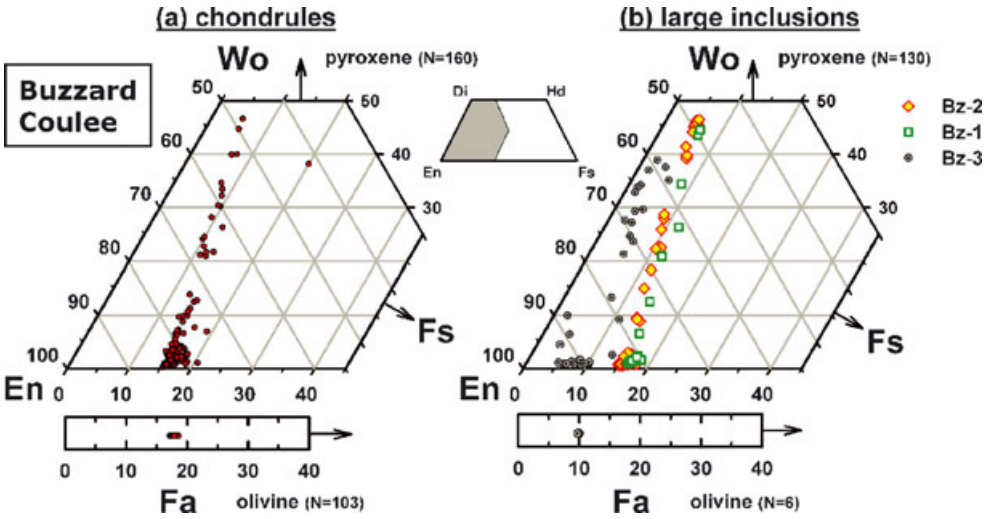

Fig. 2. Pyroxene quadrilateral and olivine plots for (a) chondrules and (b) large inclusions in Buzzard Coulee. Bz-1 and Bz-2 have pyroxene compositions that spread along an apparent mixing line similar to that observed for chondrules in the host (see also Hutson et al. 2009), whereas both pyroxene and olivine compositions in Bz-3 are distinctly less ferroan than those found elsewhere in the meteorite.

and Co, measured trace elements tend to be depleted in cristobalite compared with feldspathic patches by a relatively uniform factor of 0.027 ± 0.019 (mean and standard deviation) (Fig. 3c).

SIMS Results for Bz-3

Trace element abundances for Bz-3 are shown in Fig. 4. High-Ca pyroxene (augite) and low-Ca pyroxene typically show similar patterns to those for the corresponding phases in Bz-2, but at higher abundances, especially for low-Ca pyroxene (Fig. 4a). Analyses of one low-Ca pyroxene core grain and the partial augite overgrowth around it show a more irregularly fractionated REE pattern (Fig. 4b). This pattern has positive Yb anomalies, negative Eu anomalies, and HREE/LREE abundances that are relatively low. The irregular patterns appear to represent a modified Group II trace element pattern. Na-rich and K-rich glasses generally have overlapping abundances except that K and Rb contents are notably higher in K-rich glass (Fig. 4c). All the glass analyses show a negative Yb anomaly, and at least two (B11-3, Na-rich; B11-4, K-rich) have a negative Sm anomaly (Fig. 4c).

DISCUSSION

Igneous Crystallization

The textures and phase chemistries of the inclusions are best explained by igneous crystallization. As explained below, such crystallization appears to have occurred with a closer approach to equilibrium for Bz-2 (white lithology) than for Bz-3 (tan lithology). We consider that Bz-1 formed in the same way as Bz-2 as it is a sample of the same lithology.

White Lithology

For Bz-2, the best evidence for a quasi-equilibrium crystallization origin is the trace element compositions of orthobronzite and diopside, which show fractionated patterns generally consistent with igneous partitioning under reducing conditions (Fig. 3a). Similarly, the positive Eu anomaly and enrichment of incompatible elements in glass are what one would expect if the glass represents residual melt after the crystallization of pyroxene with negative Eu anomalies (Fig. 3c). Moreover, a comparison of C_{orbr}/C_{diop} ratios with D_{opx}/D_{cpx} values (where C_{phase} = the measured concentrations for orthobronzite and diopside and $D_{mineral}$ = the equilibrium mineral/melt partition coefficients given by Ruzicka and Hutson (2010) for orthopyroxene and clinopyroxene) suggests that orthobronzite and diopside in Bz-2 are close to being in equilibrium with one another for most elements. Exceptions include the LREE, Sr, and Al (relative excess in orthobronzite), possibly Rb (excess in diopside, but D-values are uncertain), and Sc and Zr (slight excess in diopside). The relatively high and flat LREE pattern for orthobronzite is notable, unlike what one would expect for igneous partitioning (Fig. 3a), and could indicate postcrystallization secondary enrichment or disequilibrium.

Unlike the data for orthobronzite and diopside, the relatively unfractionated trace element pattern of

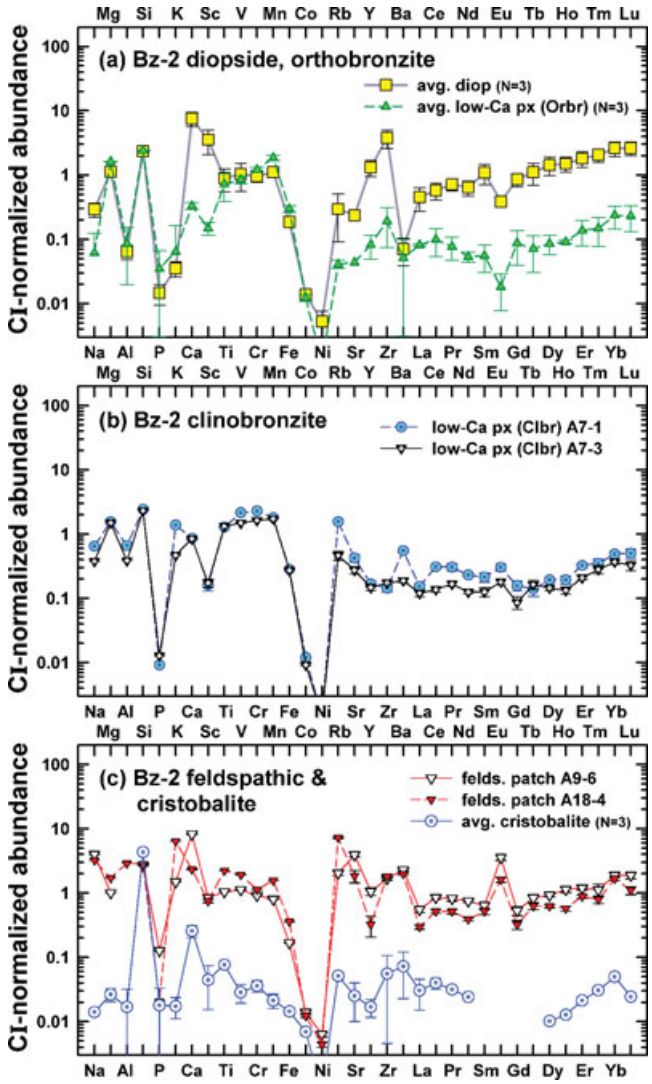

Fig. 3. CI-chondrite-normalized abundance plots for phases in Bz-2. N = number of analyses averaged; error bars indicate ± 1 standard deviation of the mean except where noted. a) Average diopside and orthobronzite. b) Two analyses of clinobronzite; error bars represent counting statistic error. c) Average cristobalite and two analyses centered on feldspathic areas ("felds. patch"). Error bars for the latter represent counting statistic error.

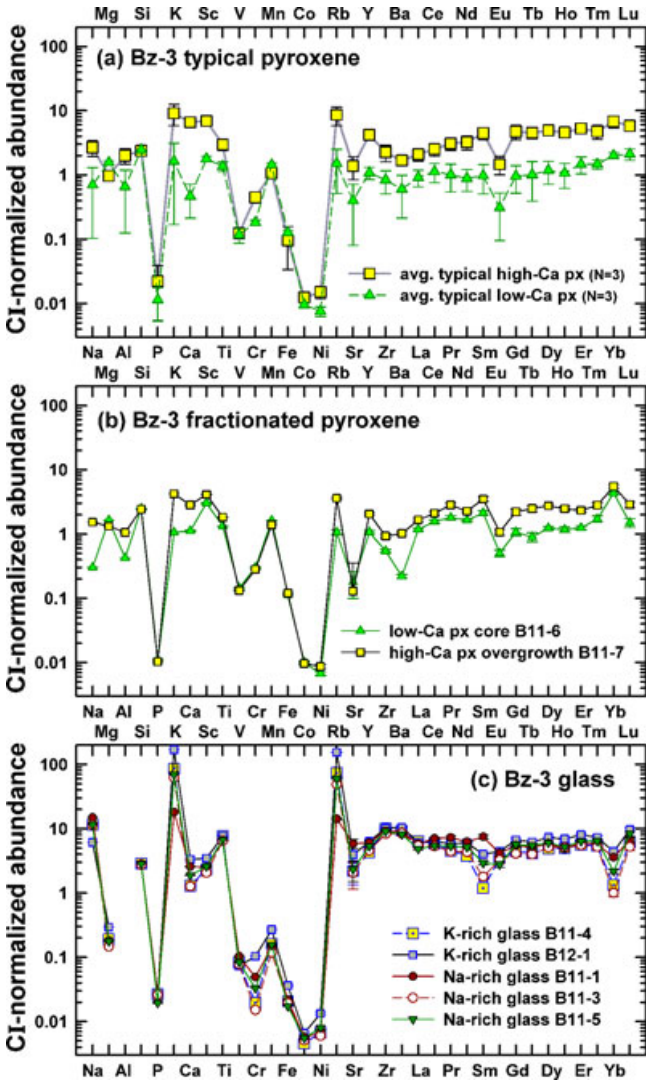

Fig. 4. CI-chondrite-normalized abundance plots for phases in Bz-3. a) Average typical low-Ca and high-Ca pyroxene (px). N = number of analyses averaged; error bars indicate ± 1 standard deviation of the mean. b) Two analyses of low-Ca and high-Ca px, representing core-overgrowth features of a single-grain cluster, have relatively fractionated REE patterns featuring positive Yb and negative Eu anomalies, and CI-normalized abundances of LREE (La-Sm) ≥ HREE (Gd-Lu except for Yb). Error bars represent counting statistic error. c) Five analyses of glass; error bars represent counting statistic error. All glasses have negative Yb anomalies; some also have negative Sm anomalies. K-rich glasses are strongly enriched (approximately 70–200 × CI) in K and Rb.

clinobronzite in Bz-2 is generally inconsistent with experimental data for equilibrium igneous partitioning (Fig. 3b). We suggest that this pattern reflects crystallization of clinobronzite under disequilibrium conditions, most likely caused by rapid cooling. This is supported by experimental data for pyroxene and olivine that show that rapid cooling results in less fractionated trace element patterns compared with an equilibrium condition (Kennedy et al. 1993).

The presence of Ca-rich rims on low-Ca pyroxene grains and cristobalite aggregates in Bz-1 and Bz-2 imply that the low-Ca pyroxene grains and silica aggregates crystallized mainly before high-Ca pyroxene. We speculate that the tendency for cristobalite to form small grains in aggregates rather than coarse grains indicates a small growth rate, but high nucleation density for this phase, relative to pyroxene. With this in mind, the comparable sizes of low-Ca pyroxene grains and

cristobalite aggregates in Bz-1 and Bz-2 could indicate roughly contemporaneous crystallization, consistent with the sequence low-Ca pyroxene + cristobalite → high-Ca px + low-Ca pyroxene. Textural evidence is ambiguous for the relative crystallization sequence of clinobronzite and orthobronzite in Bz-1 and Bz-2.

Tan Lithology

For Bz-3, the best evidence for igneous crystallization is the texture of the inclusion (Figs. 1c–d and 1h). Overgrowth and microporphyritic textures imply that the crystallization sequence in this inclusion was olivine → low-Ca pyroxene → high-Ca pyroxene → plagioclase + pyroxene. The distinct regions of Na- and K-rich glass may have formed by immiscible separation of Na- and K-rich melts, as has been proposed for silicate inclusions in the Sombrerete iron meteorite (Ruzicka et al. 2006).

The fractionated trace element patterns for most pyroxene in Bz-3 are generally consistent with igneous partitioning (the LREE in low-Ca pyroxene again being a notable exception) (Fig. 4a). But unlike for Bz-2, low- and high-Ca pyroxene grains in Bz-3 are not in equilibrium: $C_{\text{low-Ca px}}/C_{\text{high-Ca px}}$ ratios show much less variation ($< 10\times$) than the approximately 2 orders of magnitude or more variation one would expect based on $D_{\text{opx}}/D_{\text{cpx}}$ ratios. This suggests a relatively strong departure from equilibrium during the crystallization of Bz-3. In addition, the presence in some pyroxene grains of Group II-like trace-element patterns is unlike that expected for simple igneous crystallization (Fig. 4b). Group II patterns are generally believed to indicate condensation phenomena (Boynton 1975, 1989; Davis and Grossman 1979), but the patterns in Fig. 4b seem to reflect a combination of a Group II signature (CI-normalized HREE < LREE mainly, positive Yb anomaly) and an igneous signature (negative Eu anomaly and CI-normalized Lu/La ≥ 1). This could indicate that the grain formed in part by condensation and in part by crystallization (possibly incorporation of a condensate in a melt). A similar origin was proposed for grains in Si-rich chondrules (SRCs) by Hezel et al. (2006). In any case, the varying REE patterns for different pyroxene grains in Bz-3 are clear evidence for disequilibrium.

Glass abundance patterns in Bz-3 are also variable, most conspicuously in the presence of variable Sm and Yb anomalies (Fig. 4c). The existence of both Yb and Sm anomalies is reminiscent of inclusions from IIE-type silicate-bearing iron meteorites (Hsu 2003; Takeda et al. 2003; Ruzicka et al. 2006). These anomalies were interpreted by the latter authors as reflecting partitioning between vapor, melt, and solids during crystallization. As with the pyroxene phenocrysts, the different glass patterns indicate that Bz-3 formed under disequilibrium conditions.

Table 4. Reconstructed bulk compositions for inclusions in Buzzard Coulee.[a]

	Bz-1	Bz-2	Bz-3
SEM + EMPA wt%			
SiO_2	67.2 (2.5)	67.3 (2.4)	61.5 (4.3)
TiO_2	0.04 (0.01)	0.06 (0.03)	0.36 (0.08)
Al_2O_3	0.23 (0.07)	0.41 (0.16)	10.47 (1.61)
Cr_2O_3	0.20 (0.08)	0.25 (0.28)	0.11 (0.03)
FeO	7.82 (0.63)	6.94 (0.60)	2.07 (0.61)
MnO	0.46 (0.04)	0.33 (0.03)	0.23 (0.03)
MgO	21.4 (1.5)	21.3 (1.5)	15.3 (2.1)
NiO	0.01 (0.02)	0.03 (0.02)	0.02 (0.01)
CaO	2.50 (1.05)	3.21 (1.23)	5.67 (1.89)
Na_2O	0.08 (0.02)	0.14 (0.04)	3.39 (0.72)
K_2O	0.01 (0.01)	0.04 (0.01)	0.92 (0.41)
Na/Al (at.)	0.59 (0.24)	0.57 (0.27)	0.53 (0.11)
Si/Al (at.)	246 (72)	137 (54)	4.9 (0.6)
Mg/Al (at.)	120 (36)	166 (26)	1.8 (0.3)
Mg/Si (at.)	0.49 (0.04)	0.48 (0.04)	0.36 (0.05)
Fe/Mn (at.)	17.2 (2.1)	20.7 (2.5)	8.83 (2.86)
Fe/Mg × 100 (at.)	20.5 (2.2)	18.3 (2.0)	7.62 (2.47)
SEM + SIMS			
Na (μg g^{-1})		1580 (200)	39450 (6040)
Mg (wt%)		10.5 (0.5)	6.07 (0.78)
Al (wt%)		0.240 (0.03)	5.73[b] (0.88)
Si (wt%)		30.7 (0.7)	28.0 (1.3)
P (μg g^{-1})		21.3 (16.8)	25.5 (6.5)
K (μg g^{-1})		248 (59)	18400 (8500)
Ca (wt%)		1.71 (0.32)	2.78 (0.71)
Sc (μg g^{-1})		4.26 (1.52)	21.0 (3.3)
Ti (μg g^{-1})		360 (65)	2080 (160)
V (μg g^{-1})		60.3 (6.8)	5.89 (0.55)
Cr (μg g^{-1})		3080 (230)	462 (99)
Mn (μg g^{-1})		2370 (180)	1220 (150)
Fe (wt%)		3.69 (0.33)	1.10 (0.33)
Co (μg g^{-1})		5.24 (0.43)	4.00 (0.31)
Ni (μg g^{-1})		20.2 (4.4)	92.5 (15.4)
Rb (μg g^{-1})		1.24 (0.28)	63.6 (30.0)
Sr (μg g^{-1})		1.80 (0.19)	18.0 (9.2)
Y (μg g^{-1})		0.497 (0.106)	6.74 (0.95)
Zr (μg g^{-1})		3.09 (0.86)	22.7 (2.0)
Ba (μg g^{-1})		0.504 (0.100)	12.6 (1.0)
La (μg g^{-1})		0.0374 (0.0076)	0.895 (0.086)
Ce (μg g^{-1})		0.135 (0.024)	2.58 (0.36)
Pr (μg g^{-1})		0.0222 (0.0029)	0.384 (0.075)
Nd (μg g^{-1})		0.0930 (0.0145)	1.84 (0.28)
Sm (μg g^{-1})		0.0406 (0.0102)	0.554 (0.244)
Eu (μg g^{-1})		0.0113 (0.0014)	0.136 (0.024)
Gd (μg g^{-1})		0.0428 (0.0083)	0.850 (0.142)
Tb (μg g^{-1})		0.00998 (0.00278)	0.151 (0.022)
Dy (μg g^{-1})		0.0836 (0.0203)	1.16 (0.13)
Ho (μg g^{-1})		0.0197 (0.0040)	0.240 (0.025)
Er (μg g^{-1})		0.0732 (0.0149)	0.805 (0.098)
Tm (μg g^{-1})		0.0128 (0.0023)	0.117 (0.014)
Yb (μg g^{-1})		0.113 (0.020)	0.598 (0.138)
Lu (μg g^{-1})		0.0166 (0.0029)	0.138 (0.024)

[a] $\pm 1\sigma$ error given in parentheses, assuming 7% relative error in modes (2% error for cristobalite) and phase composition error equivalent to the standard deviation of mean values.

[b] Assumes EMPA values for glasses.

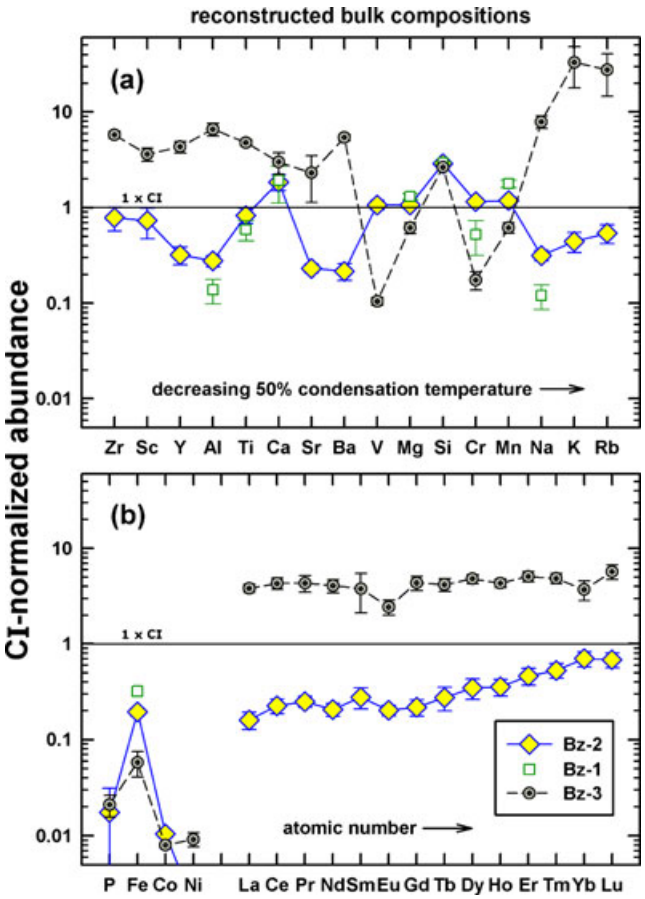

Fig. 5. Bulk CI-chondrite-normalized abundances for Bz-1, Bz-2, and Bz-3 determined by modal reconstruction (Bz-1 combines SEM + EMPA data; Bz-2 and Bz-3 combine SEM + SIMS data). Error bars show ±1σ propagated errors. a) Elements arranged according to volatility (50% condensation temperatures). b) Elements arranged according to atomic number.

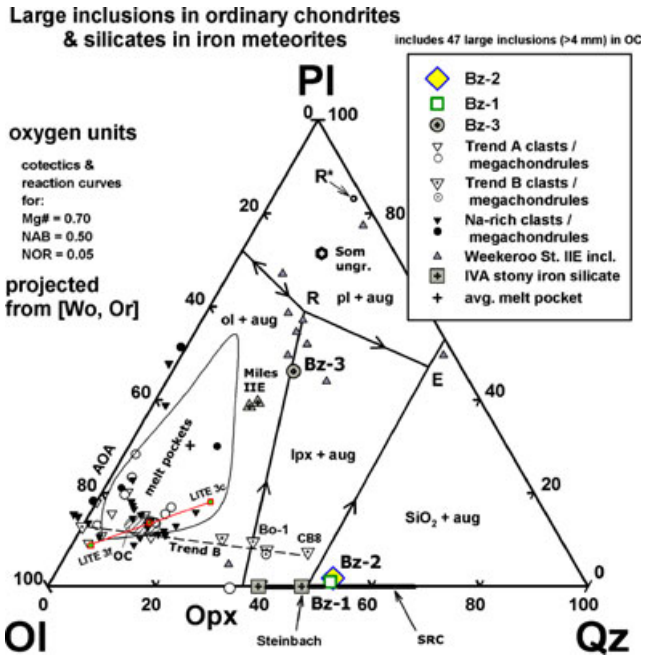

Fig. 6. Olivine (Ol)–quartz (Qz)–plagioclase (Pl) ternary liquidus diagram (Longhi 1991; algorithm given in Ruzicka et al. 1999) showing the bulk compositions of Bz-1, Bz-2, and Bz-3 compared with other large (>4 mm diameter) inclusions in ordinary chondrites (Ruzicka et al. 1995, 1998, 2000), bulk ordinary chondrites (OC, ruled area, based on Jarosewich 1990), melt pockets in OC (Dodd and Jarosewich 1982), and silicates in iron meteorites including Miles (two points show compositions of large inclusion Miles-10 and Miles 1–9 composite, Ruzicka and Hutson 2010), Weekeroo Station inclusions (Ruzicka et al. 1999), average Sombrerete inclusion (Som ungr., Ruzicka et al. 2006), and the two IVA stony-irons Steinbach and São João Nepomuceno (Ruzicka and Hutson 2006). Two points are shown for the composite large inclusion LITE 3, a fine (LITE 3f) and coarse (LITE 3c) facies (Jamsja and Ruzicka 2010). "AOA" is the average composition for AOAs in CV chondrites (Ruzicka et al. 2012); "SRC" is the range of compositions for silica-rich chondrules (Hezel et al. 2006). Other phase symbols: aug = augite, lpx = low-Ca pyroxene, SiO_2 = silica mineral; NAB = normative albite, NOR = normative orthoclase; E is the eutectic; R is the olivine–pyroxene–feldspar peritectic, R* is the peritectic in a system with Mg# = 1 and NAB = 1.

Cooling History

As discussed above, there is clear evidence based on measured trace element compositions for disequilibrium in the formation of the inclusions, especially for the tan lithology (Bz-3). The white lithology (Bz-2) has contrary indicators for equilibrium and disequilibrium. Disequilibrium could have originated by rapid cooling, with faster cooling overall for the tan lithology than for the white lithology. Additional evidence for the cooling history of the inclusions is provided by pyroxene geothermometry and the polytypes of pyroxene and silica that are present.

We used the two-pyroxene geothermometer (Lindsley 1983; Lindsley and Anderson 1983) to estimate pyroxene closure temperatures (Table 2). For Bz-3, there is a large discrepancy between low-Ca pyroxene, which records a subsolidus temperature (831 ± 61 °C; mean ± standard deviation), and high-Ca pyroxene, which records igneous temperatures (>1100 °C). This difference between low- and high-Ca pyroxene is plausibly ascribed to a higher closure temperature for high-Ca pyroxene together with rapid cooling from above the solidus. For Bz-2, in contrast, low-Ca pyroxene and high-Ca pyroxene record identical and low temperatures (752 ± 15 °C and 747 ± 47 °C, respectively), based on analyses of low-Wo and high-Wo end members. Similar low temperatures are implied for Bz-1 using a smaller dataset (Table 2). This suggests a closer approach to equilibrium in Bz-1 and Bz-2 than for Bz-3, caused by a slower cooling rate overall for Bz-1 and Bz-2.

The presence of clinobronzite instead of orthobronzite alone in Bz-1 and Bz-2, however, probably signifies rapid cooling at high temperatures. Clinobronzite can form by shearing forces during shock (transformation from orthobronzite to clinobronzite), or by relatively rapid cooling at temperatures >980 °C (transformation of protopyroxene to clinobronzite) (Huebner 1980). A shock origin for the clinobronzite is possible, but seems unlikely, as there is evidence for only modest shock in Buzzard Coulee in general, and no clear evidence for shock in the inclusions other than brecciation. On the other hand, rapid cooling seems counter to the evidence for low-temperature equilibration.

We suggest that for Bz-1 and Bz-2, rapid cooling at high temperatures (>980 °C, and possibly above the solidus—Ruzicka and Hutson 2006) was followed by slow cooling. Rapid cooling at high temperature is recorded by the presence and composition of clinobronzite, whereas slow cooling at lower temperature is recorded by the presence and composition of orthobronzite and diopside.

Cristobalite is common in some volcanic rocks and is a liquidus silica phase at low pressure (Deer et al. 1992; Gaines et al. 1997). The presence of this mineral in the white lithology is consistent with crystallization from a melt and metastable preservation during cooling. The silica phases are known to have sluggish transformation kinetics (Deer et al. 1992; Gaines et al. 1997), making feasible the preservation of cristobalite at lower temperature.

Origin of Buzzard Coulee Inclusion Melts

Igneous processes clearly played a dominant role in establishing the textures, mineralogies, and phase compositions of the inclusions. The larger question is what process created the inclusion melts in the first place. Melting of vapor-fractionated condensate mixtures, igneous differentiation, and shock melting of chondritic materials have all been suggested (see Introduction). To address this question, we consider the bulk compositions of the inclusions as calculated by modal reconstruction (Table 4). Figure 5 shows CI-normalized abundances for major and trace-element elements in the bulk inclusions, and Fig. 6 is a liquidus diagram showing the compositions of Bz-1, Bz-2, and Bz-3 compared with previously studied large (>4 mm diameter) inclusions from ordinary chondrites, as well as with other possibly related meteoritic materials.

Figure 5 illustrates that all three inclusions have high abundances of Si and low abundances of siderophile elements (especially P, Co, Ni), although the compositions are otherwise very different between Bz-3 on one hand and Bz-1 and Bz-2 on the other. Figure 6 indicates that the inclusions have major-element bulk compositions far removed from ordinary chondrite (OC) silicate, but in different ways.

Based on total Si and alkali content, Bz-3 is andesitic in overall composition. The composition of Bz-3 does not resemble that of any other large OC inclusion, but does resemble the composition of silicates in the Weekeroo Station and Miles IIE silicate-bearing irons (Ruzicka et al. 1999; Ruzicka and Hutson 2010) (Fig. 6).

The compositions of Bz-1 and Bz-2 lie close to the Si-rich extreme of Na-poor (low Na/Al) Trend B large clasts and megachondrules (Ruzicka et al. 1998, 2000), but have less normative feldspar (Fig. 6). Their composition is similar to the mean composition of silica-rich chondrules (SRCs) in ordinary chondrites (Hezel et al. 2006) and also resembles that of silicate in the Steinbach IVA stony iron (Ruzicka and Hutson 2006).

Below we evaluate different mechanisms for creating the Buzzard Coulee inclusion melts.

Formation as Shock Melts

The Buzzard Coulee inclusions have compositions that do not overlap the composition of melt pockets in ordinary chondrites, which formed by in situ shock melting (Fig. 6). Nor do the inclusions have compositions which lie on an extension of the feldspar-enrichment trend that is characteristic of incipient shock melting (Fig. 6, Ruzicka et al. 1998, 2000). Instead, the compositions of the inclusions relative to ordinary chondrites are either (1) strongly enriched in normative quartz and strongly depleted in feldspar (Bz-1 and Bz-2), which is totally unlike melt pockets or (2) enriched mainly in normative feldspar component but also in pyroxene (Bz-3) (Fig. 6). These differences suggest that the inclusions did not form by shock melting.

Ruzicka et al. (1998, 2000) inferred that Na-rich (high Na/Al) large clasts and megachondrules in ordinary chondrites could have formed by shock melting. Most of these inclusions have compositions similar to bulk ordinary chondrites except for being depleted in metal and sulfide, and although some are feldspathic, they tend not to be enriched in normative quartz (Fig. 6). Jamsja and Ruzicka (2010) described one large (approximately 3.5×4.5 mm across) igneous-textured enclave (LITE 3) in the LL chondrite NWA 4869, which they interpreted to be a rare example of a shock melt that differentiated in situ, with one side of the enclave (coarse lithology) evidently crystallizing from residual liquid after rapid crystallization of olivine in the other side (fine lithology). Although the LITE 3 liquid corresponding to the coarse lithology lies closer to the quartz apex than other inclusions interpreted to have formed by shock melting, it too lies within the melt pocket field (Fig. 6). A much larger fractionation would

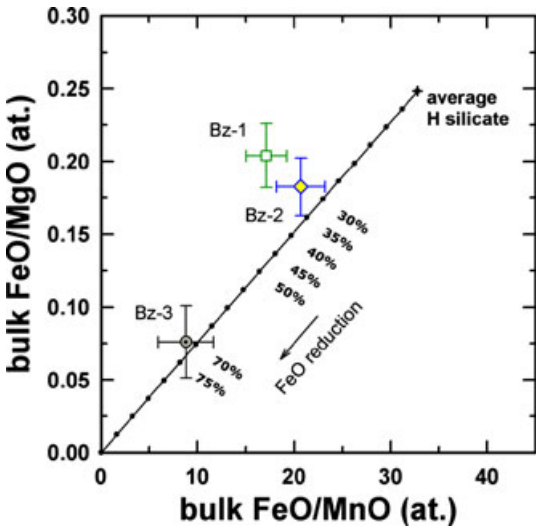

Fig. 7. Bulk FeO/MnO versus FeO/MgO for Bz-1, Bz-2, and Bz-3 compared with average H chondrite silicate (Jarosewich 1990) and an FeO reduction trajectory from average H silicate (numbers refer to % FeO reduced).

be needed to be consistent with the composition of the Buzzard Coulee inclusions.

Although we acknowledge the possibility that the white and tan lithologies in Buzzard Coulee could have formed by shock melting in ways dissimilar to that previously established, we conclude that there is no evidence that the Buzzard Coulee inclusions formed by shock melting.

Formation as Condensates

None of the Buzzard Coulee inclusions have bulk compositions suggestive of a strong volatility control, contrary to what one would expect if the inclusions formed as condensates or as mixtures of condensates.

Bz-3 is enriched in both refractory trace elements (Zr-Ba, REE), volatile elements (Na, K, Rb), and nonrefractory Si, and is depleted in ferromagnesian elements (Mg, Cr, Mn, and especially V and Cr) (Fig. 5). This abundance pattern suggests that Bz-3 is primarily enriched in incompatible elements, more consistent with formation as a partial melt than as a condensate.

On the other hand, there are features of Bz-3 that cannot be easily explained by igneous processes alone. These include an apparent negative Yb anomaly for the bulk Bz-3 composition (Fig. 5), negative Yb and Sm anomalies for glasses (Fig. 4c), and modified Group II-like patterns for some pyroxene grains (Fig. 4b). We interpret the chemical features of Bz-3 as indicating that condensation was not the dominant formation process, but that some vapor phase partitioning did occur.

The bulk abundances of Bz-2 and Bz-1 also show no obvious relationship with volatility (Fig. 5). Ruzicka et al. (1998, 2000) suggested that Trend B large clasts and megachondrules, which are slightly more feldspathic, but nearly as Si-rich as Bz-1 and Bz-2, formed by the removal of a refractory, olivine-rich condensate similar in composition to amoeboid olivine aggregates (AOAs). A similar model can account for SRCs (Brigham et al. 1986; Krot and Wasson 1994; Hezel et al. 2006). However, AOA removal alone cannot account for the compositions of Bz-1 and Bz-2. Removal of a typical AOA composition (Ruzicka et al. 2012) should result in a relatively uniform depletion of refractory elements (Zr-V, REE) relative to Si, not the factor of approximately 10 × difference in abundance of refractory elements observed for Bz-2 and Bz-1, ranging from approximately 2 x CI for Ca, to approximately 0.1–0.4 × CI for Al, Sr, Ba, Y, and many REE (La-Ho) (Fig. 5). Indeed, the Ca content of these inclusions overlaps that of AOAs (Ruzicka et al. 2012), which argues that Bz-1 and Bz-2 cannot simply represent material left over by removal of an AOA condensate. Although we consider removal of an AOA-like condensate as unpromising, we cannot rule out the possibility that condensation was involved in some way for the inclusions in Buzzard Coulee. However, the fractionated compositions of Bz-1 and Bz-2 are more suggestive of pyroxene-melt partitioning, as depletions occur in those refractory and volatile elements that are most incompatible in pyroxene. This is more consistent with the formation of Bz-2 and Bz-1 as a pyroxene-rich partial melt residue or as a cumulate than as a condensate.

Formation as Differentiates

Bz-3 probably formed as a partial melt. The Bz-3 composition appears to lie on the olivine–pyroxene reaction curve, although the exact correspondence of Bz-3 with this curve is likely fortuitous, as its position depends on a specific choice of Mg# and normative feldspar composition (Fig. 6). Nonetheless, the major-element composition of Bz-3 can be explained by partial melting of a chondrite with sufficient melting to exhaust plagioclase in the source region. This would move liquids from peritectic point R in Fig. 6 up the reaction boundary to the appropriate composition for Bz-3.

Bz-1 and Bz-2 could have originated as cumulates of a silica-rich melt. The Bz-1 and Bz-2 compositions lie close to the low-Ca pyroxene–silica cotectic (Fig. 6). This near-cotectic composition could be a coincidence, but it would be the composition expected for a cumulate that formed by crystallization on the cotectic. As previously noted, the textures of Bz-1 and Bz-2 can be explained by concurrent crystallization of pyroxene and cristobalite. Thus, a cotectic origin for Bz-1 and Bz-2 is consistent

Table 5. Petrogenesis of Buzzard Coulee inclusions.

	Bz-1 & Bz-2		Bz-3		
Process	Setting	Evidence	Process	Setting	Evidence
1. Partial melting ± metal loss	Parent body	Pyroxene trace element compositions; lack of metal	1. Partial melting ± metal loss	Parent body	Bulk composition; lack of metal
2. FeO reduction + metal loss + olivine loss	Space environment	Bulk FeO/MnO; lack of metal; Si-oversaturated composition; presence of some clinobronzite	2. FeO reduction + metal loss + vapor fractionation	Space environment	Bulk FeO/MnO; Fa & Fs contents; lack of metal; Yb & Sm anomalies & Group II patterns
3. Crystallization + crystal accumulation	Parent body	Textures; cotectic mineralogy & bulk composition; pyroxene compositions	3. Alkali metasomatism + solidification	Space environment or near-surface parent body	High bulk alkali contents; textures; pyroxene compositions
4. Removal of feldspathic melt	Parent body	Near absence of feldspar; bulk composition			

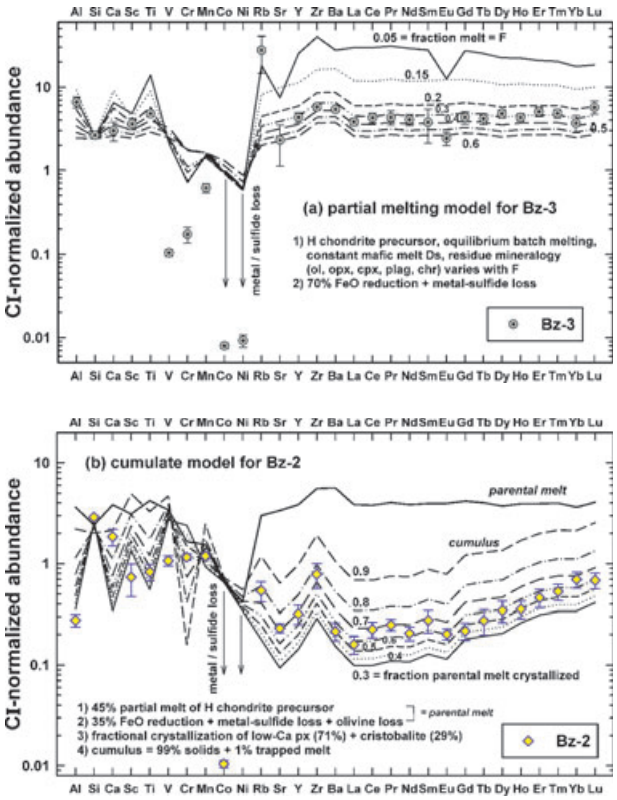

Fig. 8. Differentiation models compared with bulk compositions for (a) Bz-3 and (b) Bz-2. See text.

with the mineralogy, bulk compositions, and textures of the inclusions.

As will be shown below, trace element data for the inclusions also can be explained by crystal–liquid fractionation. We use such data to model the petrogenesis of the inclusions (see the Petrogenesis of the Inclusions section).

Metal Loss and FeO Reduction

It is clear that all of the inclusions must have experienced metal and sulfide loss, if they were derived from a chondritic precursor. All lack metal and sulfide and are significantly depleted in siderophile elements (P, Fe, Co, Ni) (Fig. 5). In addition, FeO/MnO and FeO/MgO values in them are low compared with H chondrite silicate, suggesting FeO reduction if they were derived from H chondrite-like precursors (Fig. 7). Even greater reduction would be needed if the inclusions were derived from L- or LL-like chondrite precursors. The relevant reaction is FeO (melt) $\rightarrow$ Fe (metal) + ½ O_2 (gas), with both metal and gas removed from the system.

The inclusions are found in an H chondrite, and derivation from an H chondrite-like protolith seems likely for Bz-1 and Bz-2, given their H-like pyroxene ferrosilite content. This scenario is also plausible for Bz-3. Although we make the assumption below of an H chondrite-like precursor for all the inclusions, this idea should be tested in the future (e.g., by obtaining oxygen-isotope data).

The composition of Bz-3 lies almost exactly on the predicted FeO reduction trend from an H chondrite-like chondritic precursor, indicating that it could have experienced conversion of approximately 70–75% FeO to metal, which was then lost (Fig. 7).

Bz-2 and especially Bz-1 lie somewhat off the reduction trend to higher FeO/MgO values (Fig. 7). This shift can be explained by igneous differentiation, which can affect FeO/MgO values much more than FeO/MnO. The data for Bz-2 and Bz-1 can be explained as derivation from H chondrite-like melts that experienced approximately 35–45% FeO reduction (causing a decrease in both FeO/MnO and FeO/MgO), followed by complete metal loss, together with olivine or pyroxene

fractionation (causing an increase in FeO/MgO and little change in FeO/MnO).

Petrogenesis of the Inclusions

Table 5 summarizes the inferred petrogeneses of the two inclusion lithologies. Both involve a major role for igneous differentiation in a parent body setting to produce an Si-enriched precursor melt, as well as a period of transit of such melt through a low-pressure, low-gravity space environment where cooling, FeO reduction, and gas phase phenomena occur. Thus, our models involve a combination of what might be considered "planetary" and "nebular" settings and processes.

Figure 8 compares the bulk trace element compositions of Bz-3 and Bz-2 to the predictions of quantitative differentiation models. These models assume a starting composition equivalent to H chondrite. This could be an actual H chondrite parent body or one chemically similar to it. The models are appropriate only to the observable silicate portions of the inclusions, and do not include metal-silicate partitioning or vapor-phase partitioning. However, they include the indirect effect of a concentration increase caused by FeO reduction and metal and troilite loss.

Below, we discuss detailed models for the inclusions, starting with the simpler inferred petrogenesis (Bz-3) and moving to the more complex (Bz-1 and Bz-2).

Petrogenesis of Bz-3

We interpret Bz-3 as having formed in an ordinary chondrite-like precursor body that was partly melted by internal differentiation (Bz-3 Step 1, Table 5). Plagioclase was completely melted and some or all metal and sulfide may have been removed at this time.

We suggest that the melt was next transported into a cold space environment where pressure was low, either as a result of pyroclastic ejection or collisional splashing (Bz-3 Step 2, Table 5). To account for the low FeO/MnO and fayalite and ferrosilite contents, an inferred 70% of the FeO in the melt was converted into metal. All the remaining metal was removed at this time, possibly by dynamic (e.g., spinning or collision-induced) processes. Some or all of the O_2 gas evolved by reduction was removed by venting to space, and the more volatile REE including Yb, Eu, and Sm were also partly lost to gas (Yb and Sm become volatile under reducing conditions—Boynton 1989; Lodders and Fegley 1993). This would account for negative Yb and Sm anomalies in the melt out which glass solidified, and for negative Eu and Yb anomalies in the bulk inclusion (Figs. 4c and 5). Some grains may have condensed from gas and been incorporated into melt as seeds for growing pyroxene crystals, accounting for Group II-like patterns in some

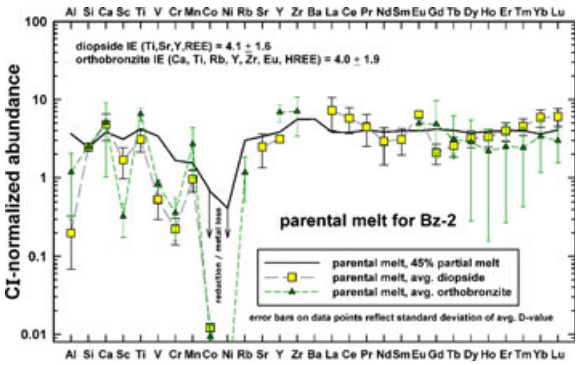

Fig. 9. Parental melt compositions calculated for Bz-2 based on average diopside (avg. diopside) and orthobronzite (avg. orthobronzite) composition and a 45% partial melt of an H chondrite (same as shown in Fig. 8b). See Text.

pyroxene (Fig. 4b). More volatile elements (e.g., alkalis, Mn, Cr) must have been partly driven into the gas at this time if the more refractory Yb, Eu, and Sm were being removed. Because the space environment was cold, the inclusion melt crystallized rapidly, resulting in various disequilibrium features.

We infer that during cooling, alkali elements that were driven into the gas re-entered Bz-3 in a process of alkali metasomatism (Bz-3 Step 3, Table 5). This process is evidenced by the high abundances of alkalis in bulk Bz-3 (approximately $30 \times$ CI for K and Rb, approximately $8 \times$ CI for Na, Fig. 5). Although it is unclear why the alkali contents are so high, it is clear that these elements must have been able to diffuse readily into Bz-3, either through melt or glass. Evidence for alkali metasomatism in the form of radial chemical gradients has been found for other large inclusions in ordinary chondrites (Ruzicka et al. 1998). For Bz-3, alkali metasomatism could have occurred either while the object was in space or near the surface of a parent body amidst an alkali-rich vapor, but probably was not caused by metamorphism in the parent body, given the evidence that Bz-3 did not equilibrate with the surrounding host materials. Finally, the Bz-3 lithology was solidified, brecciated, and incorporated into the Buzzard Coulee source region.

Modeling the differentiation of Bz-3, we equate the reconstructed bulk composition to a melt composition. Models indicate that this composition is similar to what one would obtain with approximately 30–40% partial melting of an H chondrite, corrected for metal loss and FeO reduction (Fig. 8a). Removal of metal and FeO is seemingly necessary to explain the high silica content of Bz-3, which is then matched almost exactly (Fig. 8a). The melting models for Bz-3 clearly fail for Co, Ni, V, Cr, Mn and to a lesser extent for Rb, Eu, and Yb

(Fig. 8a). The large discrepancy for Co and Ni obviously reflects the incorporation of these elements into metal that was removed from the system. The discrepancies for Eu, Yb, and possibly Mn can be explained by partial loss of these elements in a vapor phase; that for Rb is attributed to alkali metasomatism after peak heating. The discrepancies in V and Cr may indicate either unrepresentative sampling of chromite in the studied section of Bz-3, the presence of chromite too small to be identified in phase maps, or retention of these elements in chromite in the source region. However, given the otherwise good agreement between modeled and observed abundances, we conclude that Bz-3 formed by approximately 30–40% silicate partial melting of an ordinary chondrite-like precursor.

Petrogenesis of Bz-1 and Bz-2

We suggest that the first step in forming Bz-1 and Bz-2 was again partial melting of an ordinary chondrite-like precursor (Bz-1 & Bz-2 Step 1, Table 5), followed by the brief transport of melt into a low-pressure, cold space environment, possibly by collisional splashing (Bz-1 & Bz-2 Step 2, Table 5). To account for the low bulk FeO/MnO, 35% of the FeO in the liquid is converted to metal and removed from the silicate melt by the same processes as inferred for Bz-3. Unlike Bz-3, olivine removal and FeO reduction drive the melt composition into a silica-oversaturated condition in which olivine is unstable. This may require metastable olivine crystallization (cf. Bridges et al. 1995) along with separation of olivine from the remaining liquid. The cold space environment causes the melt to cool relatively rapidly at first.

We infer that the Bz-1 and Bz-2 precursor melt soon began to cool slowly, allowing additional differentiation to occur. Such slow cooling suggests re-accumulation of the melt into a parent body which afforded some thermal insulation (Bz-1 & Bz-2 Step 3, Table 5). This parent body may have been a secondary one, consisting of re-accumulated melt with or without entrained crystals. Depending on the amount of metastable olivine crystallization, either low-Ca pyroxene or cristobalite could become a liquidus phase, and subsequent crystallization of this phase would drive the residual liquid composition to the pyroxene–silica cotectic. Both low-Ca pyroxene and cristobalite would then crystallize in proportions similar to those observed in the inclusions, and high-Ca pyroxene ultimately would join the crystallization sequence, forming a cumulus pile consisting of pyroxene and cristobalite together with interstitial, feldspathic melt. Cooling was sufficiently slow at this stage to foster equilibrium between low-Ca and high-Ca pyroxene.

The interstitial melt has to be largely removed to account for the low abundance of feldspar (Bz-1 & Bz-2 Step 4, Table 5). Such removal could have occurred during crystallization, with residual intercumulus liquid being expelled from a cumulus pile as a result of normal buoyancy effects in a gravitational field (if the parent body was large), or by surface tension effects drawing residual liquid away (if the parent body was small). Finally, the rock solidified and was brecciated before becoming incorporated into the Buzzard Coulee source region.

Modeling the differentiation of Bz-2, we consider that the assemblage formed by crystallization from a parental melt that was derived by the partial melting of a precursor with chondritic composition. The degree of silicate partial melting is estimated as 45%, taking into account metal and FeO loss, which would produce a parental melt enriched in incompatible elements by approximately 4 × CI (Ti, Sr, Y, REE) to approximately 6 × CI (Zr, Ba) (Fig. 8b).

The parental melt composition can be assessed in an independent and straightforward manner for orthobronzite and diopside in Bz-2 by using the equation $C_{melt} = C_{mineral}/D_{mineral}$, omitting elements such as the LREE in orthobronzite that appear to reflect disequilibrium or secondary exchange, or which give implausible results. The parental melt composition so determined is uncertain owing to uncertainties in *D*-values, but the results for orthobronzite and diopside are mostly consistent with the assumed 45% partial melt (Fig. 9). For incompatible elements (IEs) in high-Ca pyroxene, the inferred parent melt composition is $4.1 \pm 1.6 \times$ CI (mean and standard deviation), whereas for IEs in low-Ca pyroxene, it is $4.0 \pm 1.9 \times$ CI (Fig. 9). These IE abundances probably represent an upper limit to the true, initial parent melt abundances, as some crystal fractionation could have occurred prior to the crystallization of the minerals analyzed in Bz-2.

These considerations suggest that Bz-2 was indeed crystallized from a high-degree partial melt and support the idea of late-stage loss of feldspathic melt. An alternative model of early loss of feldspathic melt, proposed by Ruzicka et al. (1995) for the Si-rich clast Bo-1 in Bovedy, would produce a melt depleted in incompatible elements, unlike the parental melt that appears to be needed for Bz-2.

Figure 8b shows the composition of a cumulus pile consisting of 99% solids + 1% trapped melt, as generated by fractional crystallization of low-Ca pyroxene and cristobalite in the proportions found in Bz-2, from the inferred parental melt of this inclusion. A value of 1% trapped melt was chosen as this is similar to the proportion of feldspathic glass in Bz-2. The models shown include the whole-scale removal of unmelted solid (olivine) from the co-existing melt, but do not include any effect of metastable crystallization of olivine from the

melt. The abundances of most elements can be adequately explained by approximately 40–80% fractional crystallization of low-Ca pyroxene + cristobalite from the parental melt (Fig. 8b). Particularly well matched for Bz-2 are the abundances of incompatible elements such as the REE, Rb, Sr, Y, Zr, Ba, and Ti, as well as more compatible elements such as Cr and Mn. The main discrepancies besides Co and Ni are for V, Sc, and Al (modeled abundances too high) and Si (modeled abundance too low). The discrepancies may be explained by some combination of (1) unaccounted fractionation by olivine, spinel, or high-Ca pyroxene; (2) uncertainties in *D*-values (especially for cristobalite); or (3) actual proportions of trapped melt and crystallizing phases that are different from the model.

We consider the most important discrepancy in the Bz-2 model to be for Si, which has model abundances low by 10–24%, for the best-fit 40–80% fractional crystallization cases (Fig. 8b). This discrepancy is most plausibly explained by metastable fractional crystallization of olivine before the crystallization of low-Ca pyroxene and cristobalite. To obtain the correct value for Si abundance implies fractional crystallization of approximately 24–54% olivine from the precursor melt prior to the crystallization of low-Ca pyroxene and cristobalite, with the lower values corresponding to more crystallization of the other phases and vice versa.

Our overall assessment is that the white lithology can be explained as being derived from a precursor of ordinary chondrite composition with a three-stage igneous model involving (1) a high degree of partial melting, (2) fractional crystallization to form a cumulate, and (3) loss of feldspathic melt, in that order. Pyroxene and cristobalite were cumulus phases from a melt that was Si-oversaturated as a result of both FeO reduction and metastable olivine crystallization.

Relationship with Differentiated Meteorites

Our data suggest a possible relationship between the inclusions in Buzzard Coulee and some differentiated meteorites. In particular, there are many important similarities between (1) the tan lithology (Bz-3) and silicates in fractionated IIE-type irons and (2) the white lithology (Bz-1 and Bz-2) and silicates in the Steinbach IVA stony iron.

As with the tan lithology, fractionated IIE-type irons (1) have bulk silicates characterized by relatively high normative feldspar and pyroxene contents compared with ordinary chondrites, which approach minimum melt compositions in a chondritic system (Fig. 6), (2) sometimes show Sm and Yb anomalies in various phases (Ruzicka et al. [2006] and references therein), (3) sometimes are glassy and contain both Na-rich and K-rich glass (Ruzicka et al. 1999, 2006), (4) sometimes show evidence for rapid cooling as manifested by discrepancies in closure temperatures for high-Ca and low-Ca pyroxene (Ruzicka et al. 1999), and (5) have a similar inferred partial melt origin, based on studies of Miles (Ruzicka and Hutson 2010), Weekeroo Station (Ruzicka et al. 1999), and Sombrerete (Ruzicka et al. 2006). Sombrerete and Weekeroo Station appear to be an especially close match, except that unlike Bz-3, Sombrerete is rich in phosphate minerals. Phosphate is also an important accessory mineral in the other IIE meteorites.

As with the white lithology, Steinbach (1) has a bulk silicate mineralogy that lies close to the pyroxene-silica cotectic, which, compared with ordinary chondrites, is enriched in both normative quartz and pyroxene and depleted in feldspar, (2) contains clinobronzite in addition to orthobronzite, (3) shows evidence for FeO reduction, and (4) is modeled as having formed as a cumulate from a Si-rich melt that was generated by a high degree of partial melting of an ordinary chondrite precursor (≥30–50% for Steinbach, 45% for Bz-2) followed by a large amount of fractional crystallization (approximately 60–70% for Steinbach, 40–80% for Bz-2) (Ruzicka and Hutson [2006] and references therein). However, in Steinbach, tridymite (not cristobalite) is the silica polymorph, and grain size is much coarser (1–2 mm across).

Another obvious difference is that in the differentiated meteorites, the silicates are associated with large amounts of metal, whereas metal is absent in the inclusions. We suggest that the inclusions and differentiated meteorites may have formed in similar ways, but that the inclusions are not simply fragments of the same identical rock types. Further study exploring this connection between differentiated and undifferentiated meteorites is clearly warranted.

CONCLUSIONS

1. The Buzzard Coulee chondrite contains at least two types of large, igneous-textured inclusions that are clasts of Si-rich igneous rocks. A tan lithology is andesitic in composition and shows evidence for having cooled relatively quickly from melt temperatures; a white lithology is a pyroxene-silica rock that appears to have crystallized rapidly at a high temperature and then cooled more slowly at a lower temperature.

2. The bulk compositions of the inclusions are dissimilar to whole rock chondrites and are not enriched in feldspar alone, suggesting that they did not form by total or partial shock melting of a chondritic precursor. Moreover, these compositions show no evidence for strong volatility control and are unlike what one would

expect if the inclusions are condensates or mixtures of condensates. Most aspects of the geochemistry of the inclusions can be explained by crystal–liquid fractionation. We suggest that the melts from which the rocks crystallized formed primarily by igneous differentiation of ordinary chondrite-like protoliths, either within melted portions of chondrite parent bodies or in bodies chemically similar to them.

3. Although igneous differentiation evidently was important in producing the siliceous melts, we suggest that both types of melts experienced a period of transit through a cold, low-pressure space environment in which cooling, FeO reduction, and interaction with a vapor occurred. Melts may have been lofted into space by excavation or splashing during collisions, or by pyroclastic volcanism, prior to re-accreting in a parent body.

4. The inclusions in Buzzard Coulee share many similarities to silicates found in IIE-type irons (tan lithology) or in IVA stony irons (white lithology). This implies that materials and processes in undifferentiated and differentiated meteorites may be more closely related than previously believed.

Acknowledgments—The authors thank Dominik Hezel, John Bridges, and Alan Rubin for constructive suggestions for revision, Ian Franchi for editorial handling, and supporters of the Cascadia Meteorite Laboratory for their donations and funding that made this research possible.

Editorial Handling—Dr. Ian Franchi

REFERENCES

Alexander C. M. O'D. 1994. Trace element distributions within ordinary chondrite chondrules: Implications for chondrule formation conditions and precursors. *Geochimica et Cosmochimica Acta* 58:3451–3467.

Anders E. and Grevesse N. 1989. Abundances of the elements: Meteoritic and solar. *Geochimica et Cosmochimica Acta* 53:197–214.

Binns R. A. 1967. An exceptionally large chondrule in the Parnallee meteorite. *Mineralogical Magazine* 36:319–324.

Boctor N. Z., Bell P. M., Mao H. K., and Kellerud G. 1982. Petrology and shock metamorphism of Papma del Infierno chondrite. *Geochimica et Cosmochimica Acta* 46:1903–1911.

Boynton W. V. 1975. Fractionation in the solar nebula: Condensation of ytrrium and the rare earth elements. *Geochimica et Cosmochimica Acta* 39:569–584.

Boynton W. V. 1989. Cosmochemistry of the rare earth elements: Condensation and evaporation processes. In *Geochemistry and mineralogy of rare earth elements*, edited by Lipin B. R. and McKay G. A. Washington, D.C.: Mineralogical Society of America. pp. 1–24.

Bridges J. C. and Hutchison R. 1997. A survey of clasts and large chondrules in ordinary chondrites. *Meteoritics & Planetary Science* 32:389–394.

Bridges J. C., Franchi I. A., Hutchison R., Morse A. D., Loing J. V. P., and Pillinger C. T. 1995. Cristobalite- and tridymite-bearing clasts in Parnallee (LL3) and Farmington (L5). *Meteoritics* 30:715–727.

Bridges J. C., Franchi I. A., Hutchison R., Sexton A. S., and Pillinger C. T 1998. Correlated mineralogy, chemical compositions, oxygen isotopic compositions and size of chondrules. *Earth and Planetary Science Letters* 155:183–196.

Brigham C. A., Yabuki H., Ouyang Z., Murrell M. T., El Goresy A., and Burnett D. S. 1986. Silica-bearing chondrules and clasts in ordinary chondrites. *Geochimica et Cosmochimica Acta* 50:1655–1666.

Davis A. M. and Grossman L. 1979. Condensation and fractionation of rare earths in the solar nebula. *Geochimica et Cosmochimica Acta* 43:1611–1632.

Deer W. A., Howie R. A., and Zussman J. 1992. *An introduction to rock-forming minerals*, 2nd ed. Harlow, UK: Prentice Hall. 696 p.

Dodd R. T. and Jarosewich E. 1976. Olivine microporphyry in the St. Mesmin chondrite. *Meteoritics* 11:1–20.

Dodd R. T. and Jarosewich E. 1982. The compositions of incipient shock melts in L6 chondrites. *Earth and Planetary Science Letters* 59:355–363.

Floss C., James O. B., McGee J. J., and Crozaz G. 1998. Lunar ferroan anorthosite petrogenesis: Clues from trace element distributions in FAN subgroups. *Geochimica et Cosmochimica Acta* 62:1255–1283.

Fodor R. V. and Keil K. 1976. A komatiite-like lithic fragment with spinifex texture in the Eva meteorite: Origin from a supercooled impact melt of chondritic parentage. *Earth and Planetary Science Letters* 29:1–6.

Gaines R. V., Skinner H. C. W., Foord E. E., Mason B., and Rosenzweig A. 1997. *Dana's new mineralogy—The system of mineralogy of James Dwight Dana and Edward Salisbury Dana*, 8th ed. New York: John Wiley & Sons Inc. 1819 p.

Hezel D. C., Palme H., Nasdala L., and Brenker F. E. 2006. Origin of SiO_2-rich components in ordinary chondrites. *Geochimica et Cosmochimica Acta* 70:1548–1564.

Higgins M. D., Herd C. D., and Walton E. L. 2011. Micro-XRF study of the Buzzard Coulee meteorite (abstract #1944). 42nd Lunar and Planetary Science Conference. CD-ROM.

Hildebrand A. R., Milley E. P., Brown P. G., McCausland P. J., Edwards W. N., Beech M., Ling A., Sarty G., Paulson M. D., Maillet L. A., Jones S. F., Stauffer M. R., Hutson M. L., and Ruzicka A. M. 2009. A bright multiple fragmentation fireball and meteorite fall at Buzzard Coulee, Saskatchewan, Canada, November 20, 2008 (abstract #MA12A-01). American Geophysical Union, Spring Meeting 2009, Toronto, Ontario, Canada.

Hsu W. 1995. Ion microprobe studies of the petrogenesis of enstatite chondrites and eucrites. Ph.D. thesis, Washington University, St. Louis, Missouri, USA.

Hsu W. 2003. Rare earth element geochemistry and petrogenesis of Miles (IIE) silicate inclusions. *Geochimica et Cosmochimica Acta* 67: 4807–4821.

Huebner J. S. 1980. Pyroxene phase equilibria at low pressure. In *Pyroxenes*, edited by Prewitt C. T. Washington, D.C.: Mineralogical Society of America. pp. 213–288.

Hutchison R., Williams C. T., Din V. K., Clayton R. N., Kirschbaum C., Paul R. L., and Lipschutz M. E. 1988. A

planetary, H-group pebble in the Barwell, L6, unshocked chondritic meteorite. *Earth and Planetary Science Letters* 90:105–118.

Hutson M. L., Ruzicka A. M., Milley E. P., and Hildebrand A. R. 2009. A first look at the petrography of the Buzzard Coulee (H4) chondrite (abstract #1893). 40th Lunar and Planetary Science Conference. CD-ROM.

Jamsja N. and Ruzicka A. 2010. Shock and thermal history of NWA 4859, an annealed impact-melt breccia of LL-chondrite parentage containing unusual igneous features and pentlandite. *Meteoritics & Planetary Science* 45:828–849.

Jarosewich E. 1990. Chemical analyses of meteorites: A compilation of stony and iron meteorite analyses. *Meteoritics* 25:323–337.

Keil K., Fodor R. V., Starzyk P. M., Schmitt R. A., Bogard D. D., and Husain L. 1980. A 3.6-b.y.-old impact melt rock fragment in the Plainview chondrite: Implications for the age of the H-group chondrite parent body. *Earth and Planetary Science Letters* 51:235–247.

Kennedy A. K., Hutchison R., Hutcheon I. D., and Agrell S. O. 1992. A unique high Mn/Fe microgabbro in the Parnallee ordinary chondrite: Nebular mixture or planetary differentiate from a previously unrecognized planetary body? *Earth and Planetary Science Letters* 113: 191–205.

Kennedy A. K., Lofgren G. E., and Wasserburg G. J. 1993. An experimental study of trace element partitioning between olivine, orthopyroxene and melt in chondrules: Equilibrium values and kinetic effects. *Earth and Planetary Science Letters* 115:177–195.

Krot A. N. and Wasson J. T. 1994. Silica-merrihuete/roedderite-bearing chondrules and clasts in ordinary chondrites: New occurrences and possible origin. *Meteoritics* 29:707–718.

Lindsley D. H. 1983. Pyroxene thermometry. *American Mineralogist* 68:477–493.

Lindsley D. H., and Anderson D. J. 1983. A two-pyroxene thermometer. Proceedings, 13th Lunar and Planetary Science Conference. *Journal of Geophysical Research* 88: A887–A906.

Lodders K. 2003. Solar system abundances and condensation temperatures of the elements. *Astrophysical Journal* 591:1220–1247.

Lodders K. and Fegley B., Jr. 1993. Lanthanide and actinide chemistry at high C/O ratios in the solar nebula. *Earth and Planetary Science Letters* 117:125–145.

Lodders K. and Fegley B., Jr. 1998. *The planetary scientist's companion*. New York: Oxford University Press. 371 p.

Longhi J. 1991. Comparative liquidus equilibria of hypersthene normative basalts at low pressure. *American Mineralogist* 76:785–800.

Petaev M. I. and Wood J. A. 1998. The condensation and partial isolation (CWPI) model of condensation in the solar nebula. *Meteoritics & Planetary Science* 33:1123–1137.

Petaev M. I. and Wood J. A. 2005. Meteoritic constraints on temperatures, pressures, cooling rates, chemical compositions, and modes of condensation in the solar nebula. In *Chondrites and the protoplanetary disk*, vol. 341, edited by Krot A. N., Scott E. R. D., and Reipurth B. San Francisco: ASP Conference Series. pp. 373–406.

Rubin A. E., Keil K., Taylor G. J., Ma M.-S., Schmitt R. A., and Bogard D. D. 1981. Derivation of a heterogeneous lithic fragment in the Bovedy L-group chondrite from impact-melted porphyritic chondrules. *Geochimica et Cosmochimica Acta* 45:2213–2228.

Ruzicka A. and Hutson M. 2006. Differentiation and evolution of the IVA meteorite parent body: Clues from pyroxene geochemistry in the Steinbach stony-iron. *Meteoritics & Planetary Science* 41:1959–1987.

Ruzicka A. and Hutson M. 2010. Comparative petrology of silicates in the Udei Station (IAB) and Miles (IIE) iron meteorites: Implications for the origin of silicate-bearing irons. *Geochimica et Cosmochimica Acta* 74:394–433.

Ruzicka A., Kring D. A., Hill D. H., Boynton W. V., Clayton R. N., and Mayeda T. K. 1995. Silica-rich orthopyroxenite in the Bovedy chondrite. *Meteoritics* 30:57–70.

Ruzicka A., Snyder G. A., and Taylor L. A. 1998. Mega-chondrules and large, igneous-textured clasts in Julesberg (L3) and other ordinary chondrites: Vapor-fractionation, shock-melting, and chondrule formation. *Geochimica et Cosmochimica Acta* 62:1419–1442.

Ruzicka A., Fowler G. W., Snyder G. A., Prinz M., Papike J. J., and Taylor L. A. 1999. Petrogenesis of silicate inclusions in the Weekeroo Station IIE iron meteorite: Differentiation, remelting, and dynamic mixing. *Geochimica et Cosmochimica Acta* 63:2123–2143.

Ruzicka A., Snyder G. A., and Taylor L. A. 2000. Geochemical and isotopic evidence bearing on the origin of large, igneous-textured inclusions in ordinary chondrites. *Antarctic Meteorite Research* 13:19–38.

Ruzicka A., Hutson M., and Floss C. 2006. Petrology of silicate inclusions in the Sombrerete ungrouped iron meteorite: Implications for the origins of IIE-type silicate-bearing irons. *Meteoritics & Planetary Science* 41: 1797–1831.

Ruzicka A., Floss C., and Hutson M. 2012. Amoeboid olivine aggregates (AOAs) in the Efremovka, Leoville and Vigarano (CV3) chondrites: A record of condensate evolution in the solar nebula. *Geochimica et Cosmochimica Acta* 79:79–105.

Takeda H., Hsu W., and Huss G. R. 2003. Mineralogy of silicate inclusions of the Colomera IIE iron and crystallization of Cr diopside and alkali feldspar from a partial melt. *Geochimica et Cosmochimica Acta* 67: 2269–2288.

Taylor G. J., Keil K., McCoy T., Haack H., and Scott E. R. D. 1993. Asteroid differentiation: Pyroclastic volcanism to magma oceans. *Meteoritics* 28:34–52.

Weisberg M. K., Smith C., Benedix G., Folco L., Righter K., Zipfel J., Yamaguchi A., and Channaoui A. H. 2009. The Meteoritical Bulletin, No. 95. *Meteoritics & Planetary Science* 44:1–33.

Zinner E. and Crozaz G. 1986. Ion probe determination of the abundances of all the rare earth elements in single mineral grains. In *Secondary ion mass spectrometry, SIMS V*, edited by Benninghoven A., Colton R. J., Simons D. S., and Werner H. W. New York: Springer-Verlag. pp. 444–446.

APPENDIX: DETAILS OF EXPERIMENTAL TECHNIQUES AND METHODS

Phase Maps and Modal Compositions

The Zeiss Sigma FE-VP SEM at Portland State University was used to create false color phase maps with spectral imaging techniques, using a silicon drift EDX detector integrated with an Oxford Instruments INCA-Wave X-ray analytical system. These maps were in turn used to determine modal proportions by processing with ColorInspector 3D plugin (v2.3) ImageJ software. The precision of the modes is estimated from repeat measurements as approximately 5–10% (relative) for most phases, and approximately 2% for cristobalite. The approach that was used placed emphasis on what was judged (based on comparison with OLM and BSE data) to be accurate phase identifications, as opposed to maximizing the number of classified pixels. Unclassified pixels derive from (1) cracks and voids, and (2) mixed compositions located on grain margins as a result of having more than one phase in a given pixel.

Quantitative Phase Analyses

Major elements were analyzed with an electron microprobe operated at 15 kV accelerating voltage, 50 nA sample current as measured in a Faraday cup, and a beam diameter of about 1 μm. Well-characterized minerals and glasses were used as standards. Accepted analyses had totals between 97 and 101 wt% (mainly 98–100%), except for some analyses of Na-glasses, which had totals of approximately 95 wt% possibly owing to beam heating and damage. Trace elements were analyzed with an ion probe using an O^- primary beam with a diameter of about 15 μm. Energy filtering was used at low mass resolution to remove complex molecular interferences, and the resulting mass spectrum was deconvolved in the mass ranges K–Ca–Sc–Ti and Rb–Sr–Y–Zr to remove simple molecular interferences that are not eliminated with energy filtering (Alexander 1994; Hsu 1995). Sensitivity factors for the REE in pyroxene are from Zinner and Crozaz (1986); those for other elements based on various silicate standards are from Hsu (1995) and are listed in Floss et al. (1998). Absolute concentrations were determined by normalizing ion signal values to concentrations determined by electron microprobe analysis, using Si as the normalizing element. Each SIMS analysis was targeted for an area with one or more electron microprobe analyses, and each analysis obtained was evaluated to take into account the possibility of analyzing off the desired target area.

Bulk Composition

Modal compositions were combined with phase compositions to determine bulk compositions by modal reconstruction. Modes measured in area % of the exposed section were assumed to be equivalent to volume %, and combined with estimated density values of phases to calculate weight fractions of phases. The following density values (ρ_{phase}, in g cm^{-3}) based on end member mineral compositions (Gaines et al. 1997) were assumed, with the values given in the first set pertaining to Bz-1 & Bz-2, and the second set to Bz-3: $\rho_{low\text{-}Ca\ pyroxene}$ = 3.31 to 3.27, $\rho_{high\text{-}Ca\ pyroxene}$ = 3.33–3.30; $\rho_{cristobalite}$ = 2.17; $\rho_{olivine}$ = 3.43; $\rho_{feldspar}$ = 2.65 (Bz-3), $\rho_{feldspathic\ phase}$ = 2.67 (Bz-1, Bz-2), $\rho_{Na\text{-}glass}$ = $\rho_{K\text{-}glass}$ = 2.4.

Differentiation Models

For differentiation models, the starting chemical composition of H chondrites as given by Lodders and Fegley (1998) and the average mineralogy of H chondrites as determined from the norm of Jarosewich (1990) were assumed. Mineral/melt partition coefficients (D-values) are those from Ruzicka and Hutson (2010), except (1) D-values for cristobalite were estimated based on cristobalite/glass concentration ratios in Bz-2 as D = 1.57 for Si and D = 0.027 for other elements; (2) D_{Ni} values for olivine, orthopyroxene, clinopyroxene, and plagioclase were taken from an unpublished database (6.0 ± 2.3, 1.06 ± 0.06, 3.0 ± 1.1, 0.05 ± 0.01, respectively), and D_{Ni} in spinel (chromite) was assumed to be the same as for Co (6.4); (3) for a few elements with missing D-values in spinel (Al, Si, Rb, Sr, Ba), spinel was not included in the calculations. Partial melting assumed batch equilibrium melting. Nonmodal melting was assumed, with the melting residue mineralogy varying by melting degree in a fashion consistent with that given in fig. 4 of Taylor et al. (1993), as modified based on the H chondrite norm to include spinel and to distinguish between low-Ca and high-Ca pyroxene. At zero degree melting, the simplified mineralogy was taken to be (in wt%) 47% olivine, 35% low-Ca pyroxene, 4% high-Ca pyroxene, 13% plagioclase, and 1% chromite. Plagioclase was assumed to be exhausted by 15% melting, high-Ca pyroxene by 20% melting, and low-Ca pyroxene and spinel by 40% melting. The liquid compositions predicted by these models were compared with the bulk composition of Bz-3 as modified by metal loss, and were used as the starting composition for melts that experienced metal and olivine loss and fractional crystallization of low-Ca pyroxene and cristobalite to create Bz-2. The same D-values as for partial melting were assumed for crystallization.

Other

The average CI chondrite composition of Anders and Grevesse (1989) was used for CI-normalized abundances. Plots showing elements arranged by condensation temperatures are based on the work of Lodders (2003), except that the relative order of condensation temperatures for Na and K were switched consistent with results from the CWPI thermodynamic program (Petaev and Wood 1998, 2005). Electron backscatter diffraction (EBSD) techniques were used to determine the identity of the silica polymorph in Bz-2, courtesy of Sreenivas Bhattiprolu at Oxford Instruments. Pyroxene geothermometry was performed by calculating adjusted En/Wo/Fs values following the procedure of Lindsley (1983) and Lindsley and Anderson (1983), and plotting these values on a digitized version of a pyroxene quadrilateral presented by these authors and interpolating between isotherms.